

Interplay of energy dependent astrophysical neutrino flavor ratios and new physics effects

POONAM MEHTA^a AND WALTER WINTER^b

^a*Raman Research Institute,*

C. V. Raman Avenue, Bangalore 560 080, India

^b*Institut für Theoretische Physik und Astrophysik,*

Universität Würzburg, 97074 Würzburg, Germany

September 19, 2018

Abstract

We discuss the importance of flavor ratio measurements in neutrino telescopes, such as by measuring the ratio between muon tracks to cascades, for the purpose of extracting new physics signals encountered by astrophysical neutrinos during propagation from the source to the detector. The detected flavor ratios not only carry the energy information of specific new physics scenarios which alter the transition probabilities in distinctive ways, but also the energy dependent flavor composition at the source. In the present work, we discuss the interplay of these two energy dependent effects and identify which new physics scenarios can be distinguished from the detected flavor ratios as a function of astrophysical parameters. We use a recently developed self-consistent neutrino production model as our toy model to generate energy dependent source flavor ratios and discuss (invisible) neutrino decay and quantum decoherence as specific new physics examples. Furthermore, we identify potentially interesting classes of sources on the Hillas plot for the purpose of new physics searches. We find that sources with substantial magnetic fields 10^3 Gauss $\lesssim B \lesssim 10^6$ Gauss, such as Active Galactic Nuclei (AGN) cores, white dwarfs, or maybe gamma-ray bursts, have, in principle, the best discrimination power for the considered new physics scenarios, whereas AGN jets, which typically perform as pion beam sources, can only discriminate few sub cases in the new physics effects. The optimal parameter region somewhat depends on the class of new physics effect considered.

^aEmail: poonam@rri.res.in

^bEmail: winter@physik.uni-wuerzburg.de

1 Introduction

Even though extraterrestrial high energy neutrino flux has not been detected yet, efforts are made to detect neutrinos from far beyond the Sun and the Supernova 1987A. Astrophysical neutrinos at high energies open up an entirely new window to infer the properties of production sites as well as neutrinos themselves. The kilometer-scale neutrino telescopes such as IceCube [1] and KM3NeT [2] are designed to detect high energy ($E \gtrsim 10^{11}$ eV) neutrinos from various astrophysical sources. Among the candidate sources, the most prominent extragalactic ones are Active Galactic Nuclei (AGNs) [3–6] and Gamma-Ray Bursts (GRBs) [7], see Ref. [8] for a review and Ref. [9] for the general theory governing photohadronic neutrino production from astrophysical sources. There are generic theoretical bounds for the diffuse neutrino flux from sources transparent as well as opaque to neutrons [10, 11]. The diffuse flux bounds from these sources are being touched by IceCube, see, *e.g.*, Ref. [12] for GRBs. Apart from that, there is also the possibility to detect point sources for which even the optical counterpart is blocked, the so-called “hidden sources” [13].

We focus on the possibility to detect the flavor of astrophysical neutrinos. Although neutrino telescopes such as IceCube can not detect the flavor of the neutrinos directly, one can, in the simplest case, make use of the two kinds of event topologies: tracks (which are induced by muons) and cascades/showers (electromagnetic and hadronic, induced by ν_e and ν_τ , respectively) to construct an observable track to cascade flavor ratio as a flavor dependent quantity. Note that this flavor ratio is defined in the spirit of the very first search for cascades from extragalactic neutrino sources, which has been very recently conducted in Ref. [14] for IceCube-22. This flavor ratio allows us to infer particle physics properties of neutrinos [15–20], extract information on the flavor mixing parameters [21–35] and identify such sources [36, 37]. Since the flux normalization drops out of this ratio, it is relatively robust with respect to astrophysical uncertainties. We will elaborate on this point further in Sec. 3.

The high energy neutrinos are conventionally expected to originate from the decay of charged pions (pion beam source) produced via photohadronic processes ($p\gamma$) or inelastic (pp) collisions. From $\pi \rightarrow \mu \rightarrow e$ decay chain, the flavor composition at the source is given by $\Phi_e^0 : \Phi_\mu^0 : \Phi_\tau^0 = 1 : 2 : 0$ (Φ_α^0 represents sum of neutrino and anti-neutrinos of a given flavor)¹. However, this picture is over-simplified and it was pointed out in Refs. [9, 39] that energy losses in strong magnetic fields, which dominantly affect the muons for a pion beam source, changes $\Phi_e^0 : \Phi_\mu^0 : \Phi_\tau^0$ to $0 : 1 : 0$ at high energies (muon damped source). This established the energy dependence of the flavor composition of a given source and one can expect a smooth transition from one type of source to another as a function of the neutrino energy [40–42], mostly depending on the cooling processes of the intermediate muons, pions and kaons (or even charmed mesons, which we do not consider). Other mechanisms, such as neutron decay, define a new class of sources, and even all special classes may be recovered as a function of energy [43]. At low energies, neutron decays may dominate the flux, where the

¹At neutrino telescopes without charge identification capability, $p\gamma$ and pp processes are indistinguishable since both lead to the same flavor composition $1 : 2 : 0$ (neutrinos and anti-neutrinos are added). However, one may use the Glashow resonance ($E \simeq 6.3$ PeV) initiated by $\bar{\nu}_e$ to discriminate between the primary processes which differ in $\pi^+ - \pi^-$ symmetry [25, 38].

neutrons are generated in the photodissociation of heavy nuclei or photohadronic interactions, which leads to $1 : 0 : 0$ (neutron beam source) [44]. If the cooled muons pile up at low energies, one may even have $1 : 1 : 0$ from muon decays only (muon beam source) [43]. A simple-minded model for implementing the photohadronic interactions in cosmic accelerators was recently developed by Hümmer, Maltoni, Winter and Yaguna [HMWY] [43]. In the HMWY model, charged pions are produced from photohadronic ($p\gamma$) interactions between protons and the synchrotron photons from co-accelerated electrons (positrons). The photohadronic interactions are computed using an efficient state-of-the-art method described in Ref. [45], based on the physics of SOPHIA [46], and the helicity-dependent muon decays from Ref. [41] are included. The toy model relies on relatively few astrophysical parameters, the most important ones being the size of the acceleration region (R), the magnetic field strength at the source (B), and the injection index (α) which is assumed to be universal for protons and electrons/positrons. In the HMWY model, the energy dependent effects mentioned above are taken into account automatically: the synchrotron cooling of all secondary species is included, as it is important for the accurate prediction of the flavor ratios at the source.

The observed neutrino flavor composition at the detector is in general different from that at source due to neutrino flavor oscillations. Standard flavor mixing leads to achromatic (energy independent) transition probability for astrophysical neutrinos because of decoherence of the oscillations. For a pion beam source and standard flavor mixings, one gets an interesting prediction of flavor equipartition $1 : 1 : 1$ at the detector ². It should be noted that there is no physical basis for this equipartition, it is purely accidental and just a consequence of the specific choice of source and the mixing matrix in the near tri-bimaximal form along with the assumption of standard mass-induced oscillations. Hence if we consider a source other than pion beam source and/or non-standard propagation effects en-route, this prediction of universal ratio changes [19]. This clearly implies that in order to infer new physics one has to be careful, and the mere departure from flavor equipartition can not serve as a guaranteed indicator of the specific class of new physics in the most general situation. The new physics effects studied in the context of high energy astrophysical neutrinos include neutrino decay [47–51], pseudo-Dirac nature of neutrinos [22, 51], violation of discrete symmetries such as CPT [51–53], Lorentz invariance violation [50, 51, 54], quantum decoherence [51, 52, 54–56], violation of unitarity of the mixing matrix [57], coupling of neutrinos to dark energy [58] and non-standard interactions [59]. However in the existing studies, the energy dependence of the flavor composition at the source has not been taken into account explicitly and many of these studies apply to only a specific source type. In the present work, we incorporate

1. Energy dependent effects in the flavor composition at the source by using the HMWY model as our toy model, and
2. Energy dependent new physics scenarios during propagation of neutrinos from source to detector.

We study their impact on the detected flavor ratios for a point source. Most importantly,

²As long as $\theta_{23} \simeq \pi/4$ and $\theta_{13} \simeq 0$, this result is robust and independent of the value of θ_{12} .

unlike the case of standard oscillations which are achromatic, the energy dependent new physics effects lead to energy dependent probabilities. Thus energy dependent observable flavor ratio is therefore an outcome of an interplay of two energy dependent effects and one has to be careful to interpret these results for the new physics searches. In order to elucidate this interplay, we explore two representative examples (a) neutrino decay, and (b) quantum decoherence.

The first non-standard possibility considered here is that of neutrino decay over astrophysical L/E scales, which sheds light on the lifetime of the neutrinos. Among the terrestrial experiments, solar neutrino data sets the strongest limit on neutrino lifetime to mass ratio $\tau^0/m \gtrsim 10^{-4}$ s/eV [47] which implies that decay of high energy astrophysical neutrinos can not be ruled out. Astrophysical neutrinos also provide a much higher (by several orders of magnitude) neutrino lifetime sensitivity due to the higher L/E ratio involved. Decay of astrophysical neutrinos has been studied in Ref. [47–49]. The other new physics scenario considered in the present work is that of quantum decoherence effects. Even though to date there is no convincing theory of quantum gravity, it is expected to give rise to distinctive signatures such as violation of Lorentz invariance, CPT violation and/or quantum decoherence [60] at low energies (compared to the Planck scale). Neutrino telescopes are particularly well-suited to probe such new physics effects in both atmospheric [61] as well as astrophysical [53, 54] neutrino fluxes. Note that some of these exotic effects are related due to the CPT theorem, for example, CPT violation implies Lorentz invariance violation but not vice-versa, and quantum decoherence can give rise to CPT violation [60]. In particular, quantum decoherence leads to evolution of pure states to mixed states via interaction with the environment of the space-time. The effect of quantum decoherence on astrophysical neutrinos has been studied in Refs. [52, 54, 56].

The paper is organised as follows. In Sec. 2, we introduce our theoretical flavor ratio framework. Then in Sec. 3, we briefly recapitulate the HMWY model and illustrate how the flavor ratios of the sources acquire their energy dependence. We introduce our energy dependent new physics effects in Sec. 4, where we also discuss their interplay with the energy dependent flavor ratios at the source and detector. Finally, we perform a systematic scan of regions of the parameter space in Sec. 5, to identify source classes which may be most useful for this application. We then summarize in Sec. 6. Note that a more detailed discussion of the quantum decoherence model can be found in Appendix A.

2 Flavor ratio framework

We begin by defining the quantities of interest for the present study: the flavor ratio at the source, propagation effects, and the flavor ratio at the detector.

2.1 Source flavor ratio

Assuming a negligible amount of ν_τ at the source³, the flavor composition is completely characterized by the ratio of the electron to muon neutrino flux

$$\widehat{X}(E) = \frac{\Phi_e^0(E)}{\Phi_\mu^0(E)}, \quad (1)$$

where $\Phi_e^0(E)$ and $\Phi_\mu^0(E)$ are the fluxes of electron and muon neutrinos without propagation effects. These correspond to the fluxes directly at the source, apart from an overall normalization, distance dependence, a possible Lorentz boost, and redshift effects. Since all these effects affect the different flavors in the same way, it is convenient to normalize to the fluxes at the detector without propagation effects $\Phi_\alpha^0(E)$. The fluxes are typically given in units of $\text{GeV}^{-1} \text{cm}^{-2} \text{s}^{-1}$ (point source) or $\text{GeV}^{-1} \text{cm}^{-2} \text{s}^{-1} \text{sr}^{-1}$ (diffuse flux). Note that we always refer to the sum of neutrino and antineutrino fluxes in the following, since we assume that the detector cannot distinguish between these.

In the literature, the following source classes are distinguished depending upon the value of \widehat{X} :

Pion beam sources produce neutrinos from charged pion and successive muon decays, such as

$$\pi^+ \rightarrow \mu^+ + \nu_\mu, \quad (2)$$

$$\hookrightarrow e^+ + \nu_e + \bar{\nu}_\mu. \quad (3)$$

This leads to $\widehat{X} \simeq 1/2$.

Muon damped sources produce neutrinos from pion decays only, *i.e.*, Eq. (2), since the muons lose energy by synchrotron radiation efficiently. This leads to $\widehat{X} \simeq 0$.

Muon beam sources The muons may pile up at lower energies, where muon decays dominate, see Eq. (3). Then we have $\widehat{X} \simeq 1$. Note that the neutrinos from semi-leptonic decays of charmed mesons in baryon rich astrophysical environments such as slow jet supernovae [63] (where pp interactions are prevalent) also lead to high energy neutrinos with $\widehat{X} \simeq 1$ [64].

Neutron beam sources The neutrons, produced by photodissociation of heavy nuclei or photohadronic interactions, decay into neutrinos by

$$n \rightarrow p + e^- + \bar{\nu}_e, \quad (4)$$

leading to $\widehat{X} \gg 1$.

³One may get a ν_τ component in some exotic scenarios, such as cosmic defects or evaporating black holes, typically at energies beyond $\sim 10^{19}$ eV. However, the HMWY model does not extend to such high energies in most cases because of the Hillas criterion [62] and synchrotron cooling of the protons limiting the maximal energy. In addition, one typically expects a diffuse flux from such objects, whereas for point sources, the angular resolution of the instrument can be used to suppress the backgrounds. Therefore, the contribution from these objects can be neglected if point source fluxes are considered.

Undefined sources Several processes compete with similar magnitudes, leading to arbitrary \widehat{X} .

Note that $\widehat{X}(E)$ is, in general, an energy dependent quantity, and these classifications only apply to certain energy ranges. A given flavor composition at source uniquely identifies a particular mechanism provided we have some information on the type of source giving rise to the neutrino flux. For instance, a muon beam source can be mimicked by a transparent source (via decay of piled up muons at low energies) or a hidden source such as slow jet supernovae (via decay of charmed mesons) where different mechanisms are responsible for arriving at $\widehat{X} \simeq 1$. In addition, the guaranteed flux of extremely high energy neutrinos from Greisen-Zatsepin-Kuzmin (GZK) process (photohadronic interaction of highest energy cosmic rays with cosmic microwave background radiation) also yields energy dependent source flavor ratios [65, 66]. Below 100 PeV, GZK neutrinos fall in neutron beam source class while above 100 PeV, GZK neutrinos are more like a pion beam source.

2.2 Standard propagation effects

We assume propagation of astrophysical neutrinos in vacuum over distances long enough such that oscillation effects become decoherent. On incorporating the propagation effects, the flavor flux changes to Φ_β^{Det} for neutrino of flavor ν_β

$$\Phi_\beta^{\text{Det}}(E) = \sum_{\alpha=e,\mu,\tau} P_{\alpha\beta}(E) \Phi_\alpha^0(E), \quad (5)$$

where for standard oscillations, we have

$$P_{\alpha\beta}(E) \equiv P_{\alpha\beta} = \sum_{i=1}^3 |U_{\beta i}|^2 |U_{\alpha i}|^2, \quad (6)$$

which is achromatic. Note that Eq. (6) depends only on the mixing angles θ_{ij} contained in the mixing matrix elements $U_{\beta i}$ of the 3×3 Pontecorvo-Maki-Nakagawa-Sakata (PMNS) neutrino mixing matrix which in the commonly adopted Particle Data Group (PDG) parametrization is given by

$$U = \begin{pmatrix} c_{12}c_{13} & s_{12}c_{13} & s_{13}e^{-i\delta_{CP}} \\ -s_{12}c_{23} - c_{12}s_{23}s_{13}e^{i\delta_{CP}} & c_{12}c_{23} - s_{12}s_{23}s_{13}e^{i\delta_{CP}} & s_{23}c_{13} \\ s_{12}s_{23} - c_{12}c_{23}s_{13}e^{i\delta_{CP}} & -c_{12}s_{23} - s_{12}c_{23}s_{13}e^{i\delta_{CP}} & c_{23}c_{13} \end{pmatrix}, \quad (7)$$

where $s_{ij} = \sin \theta_{ij}$ and $c_{ij} = \cos \theta_{ij}$ and δ_{CP} is the Dirac type CP phase. Unless noted otherwise, we use the following values for the mixing parameters, see, *e.g.*, Ref. [67]:

$$\sin^2 \theta_{23} = 0.5, \quad \sin^2 \theta_{12} = 0.318, \quad \sin^2 \theta_{13} = 0. \quad (8)$$

Thus, we note that flavor equipartition at the detector $\Phi_e^{\text{Det}} : \Phi_\mu^{\text{Det}} : \Phi_\tau^{\text{Det}} = 1 : 1 : 1$ is a consequence of two inputs: the source ratio $\widehat{X} \sim 0.5$ (pion beam source) and the use of mixing angles being close to the tri-bimaximal form.

2.3 Flavor ratio at the detector

We need to take into account the propagation effects, before computing the observable flavor ratios at the detector. Ideally one would want to detect all the flavors separately, however in practice it is not so easy. Several flavor ratios have been constructed in literature to distinguish between flavors [20]. The easiest possibility to measure flavor ratios at neutrino telescopes requires, apart from muon tracks sensitive to ν_μ , the identification of cascades [14]. These come with a lower statistics and have a higher threshold (about 1 to 10 TeV in IceCube). In addition, the neutrino effective area increases much weaker with energy, which means that the best statistics may be obtained close to the threshold. However, one expects a much better energy resolution for cascades. If we assume that electromagnetic (from ν_e) and hadronic (from ν_τ) cascades do not need to be distinguished, a useful observable is the ratio of muon tracks to cascades [23]

$$\widehat{R} \equiv \frac{\Phi_\mu^{\text{Det}}}{\Phi_e^{\text{Det}} + \Phi_\tau^{\text{Det}}} = \frac{P_{e\mu}(E) \widehat{X}(E) + P_{\mu\mu}(E)}{[P_{ee}(E) + P_{e\tau}(E)] \widehat{X}(E) + [P_{\mu e}(E) + P_{\mu\tau}(E)]}. \quad (9)$$

Note that the above formula holds even if unitarity is violated, *i.e.*, $P_{e\alpha} + P_{\mu\alpha} + P_{\tau\alpha} < 1$, such as for neutrino decay into invisible states. In addition, note that neutral current events will also produce cascades, which, in practice, have to be included as background. In Ref. [14], the most recent IceCube cascade analysis, the contribution of the different flavors for a E^{-2} extragalactic test flux with equal contributions of all flavors at the Earth was given as: electron neutrinos 40%, tau neutrinos 45%, and muon neutrinos 15% (after all cuts). This implies that charged current showers dominate and that electron and tau neutrinos are detected with comparable efficiencies, *i.e.*, that Eq. (9) is a good first approximation to discuss flavor at a neutrino telescope. The benefit of this flavor ratio is that the normalization of the source drops out. In addition, it represents the experimental flavor measurement with the simplest possible assumptions. Eq. (9) implies that the observable flavor flux ratio \widehat{R} depends on two energy dependent quantities: $\widehat{X}(E)$ characterizing the energy dependence of the flavor composition at the source, and $P_{\alpha\beta}(E)$ characterizing the energy dependence during the propagation from source to detector. In the absence of energy dependent new physics, the probability is independent of energy (see Eq. (6)) and the flavor ratio \widehat{R} closely follows the energy dependence of the source function $\widehat{X}(E)$.

Using Eq. (6) in Eq. (9), we have listed the characteristic values of flavor ratios \widehat{X}, \widehat{R} in Table 1 assuming standard oscillations and best-fit values of oscillation parameters. In this study, we do not consider the uncertainties coming from the oscillation parameters, since we expect that the discussed measurements are only feasible with sufficient statistics on a timescale when the oscillation parameters are sufficiently limited; see discussion in Ref. [43] (Fig. 11).

3 Energy dependent flavor ratios at the source

The HMWY model describes neutrino production via photohadronic ($p\gamma$) processes for transparent sources (optically thin to neutrons) and includes the cooling of the secondary

Source	\widehat{X}	\widehat{R}
Muon damped	0	0.64
Pion beam	0.5	0.50
Muon beam	1	0.44
Neutron beam	$\gg 1$	0.28
Undefined	Other	Other

Table 1: Characteristic values of flavor ratios \widehat{X} and \widehat{R} for the considered source classes for best-fit values of oscillation parameters. The ratio \widehat{R} is computed using Eq. (9) and standard oscillation probabilities (Eq. (6)).

particles. It can be used to generate neutrino fluxes as a function of few astrophysical parameters. Below we outline the key ingredients of the model and the main results, for details see Ref. [43, 45]. All of the following quantities refer to the frame where the target photon field is isotropic, such as the shock rest frame (SRF).

3.1 Ingredients of the HMWY model

The protons and electrons/positrons are injected with spectra $\propto E^{-\alpha}$. The maximal energies of these spectra are determined by balancing the energy loss and acceleration timescale given by

$$t_{\text{acc}}^{-1} = \eta \frac{c^2 e B}{E}, \quad (10)$$

with η an acceleration efficiency depending on the acceleration mechanism, where we choose $\eta = 0.1$ later. If synchrotron losses dominate, the maximal energy is therefore given by

$$E_{\text{max}} = \sqrt{\frac{9\pi\epsilon_0 m^4 c^7 \eta}{e^3 B}}. \quad (11)$$

It scales $\propto m^2$, which means that the protons are accelerated to much higher energies, and $\propto 1/\sqrt{B}$, which means that strong magnetic fields limit the maximal energies. For each particle species, the injection and energy losses/escape are balanced by the steady state equation

$$Q(E) = \frac{\partial}{\partial E} (b(E) N(E)) + \frac{N(E)}{t_{\text{esc}}}, \quad (12)$$

with $t_{\text{esc}}(E)$ the characteristic escape time, $b(E) = -E t_{\text{loss}}^{-1}$ with $t_{\text{loss}}^{-1}(E) = -1/E dE/dt$ the rate characterizing energy losses, $Q(E)$ the particle injection rate $[(\text{GeV s cm}^3)^{-1}]$ and $N(E)$ the steady particle spectrum $[(\text{GeV cm}^3)^{-1}]$. For all charged particles, synchrotron energy losses and adiabatic cooling are taken into account. In addition, unstable secondaries, *i.e.*, pions, muons, and kaons, may escape via decay. As a consequence, for pions, muons, and kaons, neglecting the adiabatic cooling, the (steady state) spectrum is loss-steepend above the energy

$$E_c = \sqrt{\frac{9\pi\epsilon_0 m^5 c^5}{\tau_0 e^4 B^2}}, \quad (13)$$

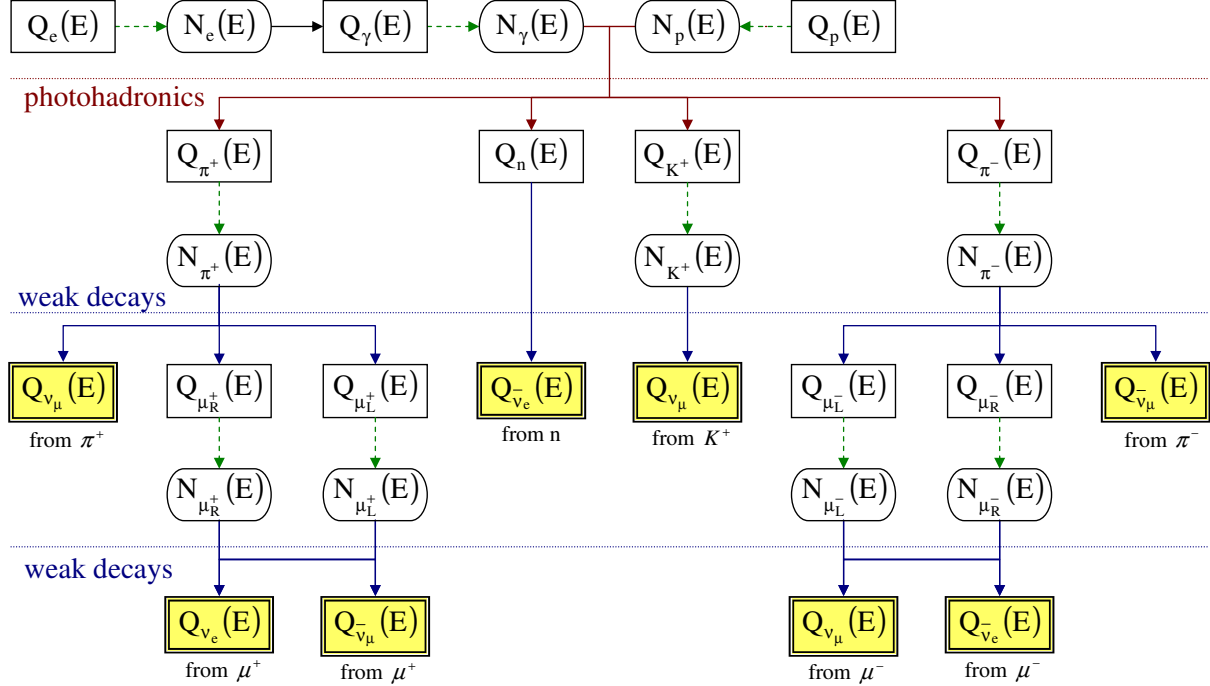


Figure 1: Flowchart describing the neutrino production in the HMWY model. The functions $Q(E)$ denote (injection) spectra per time frame $[(\text{GeV s cm}^3)^{-1}]$ and $N(E)$ steady spectra $[(\text{GeV cm}^3)^{-1}]$ derived from the balance between injection and losses or escape. Dashed arrows stand for solving the steady state differential equation Eq. (12), the horizontal line “photohadronics” to solving Eq. (16) for all interaction types. Figure taken from Ref. [43].

where synchrotron cooling and decay rates are equal. One can read off this formula that the different secondaries, which have different masses m and rest frame lifetimes τ_0 , will exhibit different break energies $E_c \propto \sqrt{m^5/\tau_0}$ which solely depend on particle physics properties and the value of B .

While being accelerated, the electrons loose energy into synchrotron photons, which serve as the target photon field. Charged meson production then occurs via

$$p + \gamma \rightarrow \pi + p', \quad (14)$$

$$p + \gamma \rightarrow K^+ + \Lambda/\Sigma, \quad (15)$$

with these synchrotron photons, where the leading kaon production mode is included and p' is a proton or neutron. In addition, two- and multi-pion production processes are included (not listed here), see Ref. [45] for details. The injection of the charged mesons is computed from the steady state proton $N_p(E_p)$ and photon $N_\gamma(\varepsilon)$ spectra with [45]

$$Q_b(E_b) = \int_{E_b}^{\infty} \frac{dE_p}{E_p} N_p(E_p) \int_{\frac{\epsilon_{\text{th}} m_p}{2E_p}}^{\infty} d\varepsilon N_\gamma(\varepsilon) R_b(x, y), \quad (16)$$

with $x = E_b/E_p$ the fraction of energy going into the secondary, $y \equiv (E_p \varepsilon)/m_p$ (directly related to the center of mass energy), a “response function” $R_b(x, y)$ (see Ref. [45]), and ϵ_{th}

the threshold for the photohadronic interactions (in terms of photon energy in the proton rest frame). The weak decays of the secondary mesons, such as Eqs. (2) and (3), are described in Ref. [41]. These will finally lead to neutrino fluxes from pion, muon, kaon, and neutron decays. The whole procedure is illustrated in Fig. 1, the finally obtained eight neutrino fluxes are shown as shaded boxes. In the following, we will sum over the fluxes from all polarities. For instance, if we refer to “ ν_μ from muon decays”, we mean the sum over the ν_μ from μ^- and the $\bar{\nu}_\mu$ from μ^+ in Fig. 1.

One can clearly see from Eq. (16), that only the product of the proton and photon (and therefore electron) density normalizations enters the final result, as long as cooling processes implicitly depending on proton-electron ratio, such as inverse Compton scattering or photohadronic cooling, are sub-dominant. This is, of course, a key simplifying assumption which, in general, limits the applicability of this model. However, it leads to the simplest possible model which includes the effects relevant for the flavor ratios, whereas additional cooling processes affecting the protons and electrons only change the shape of the neutrino spectra (including maximal energies), but not the flavor ratios as a function of energy directly. In the flavor ratios, the overall normalization from Eq. (16) cancels. In that sense, the flavor composition might be the most robust prediction one can make for a source, since it is very little affected by astrophysical uncertainties as long as the dominating cooling process of the secondaries (pions, muons, kaons) is synchrotron emission, and the dominant escape process is decay. These processes depend, however, on the magnetic field in the source B , a quantity, which is not directly accessible.

In the following, for the sake of simplicity, we assume that we can estimate the parameters of the source by utilizing the multi-messenger connection (such as gamma-ray observations). For example, one can estimate the magnetic field B from energy equipartition, the injection index from the spectral shape, and the size of the acceleration region R from the variability timescale. Then one can predict the flavor ratios as a function of these parameters. Conversely, flavor ratio measurements may provide a direct handle on astrophysical quantities such as the magnetic field [43]. We use $\alpha = 2$, since we do not obtain strongly qualitatively different results in the range $2 \lesssim \alpha \lesssim 3$.

3.2 Hillas criterion and source classification on the Hillas plot

The parameters R and B can be directly related to the Hillas plot, see Fig. 2, left panel, for an example. In order to confine a particle in a magnetic field at the source, the Larmor radius has to be smaller than the extension of the acceleration region R . This can be translated into the Hillas condition for the maximal attainable energy [62]

$$E_{\max} [\text{GeV}] \simeq 0.03 \cdot \eta \cdot Z \cdot R [\text{km}] \cdot B [\text{G}], \quad (17)$$

where Z is the charge (number of unit charges) of the accelerated particle, B is the magnetic field in Gauss, and η can be interpreted as an efficiency factor or linked to the characteristic velocity of the scattering centers. One complication in this type of figure is that R and B in Eq. (17) are potentially given in the SRF, whereas E_{\max} is to be determined in the observer’s frame. If the particles are accelerated in a relativistically moving environment, such as in a GRB fireball, this assignment is not trivial anymore, and the relatively large Lorentz

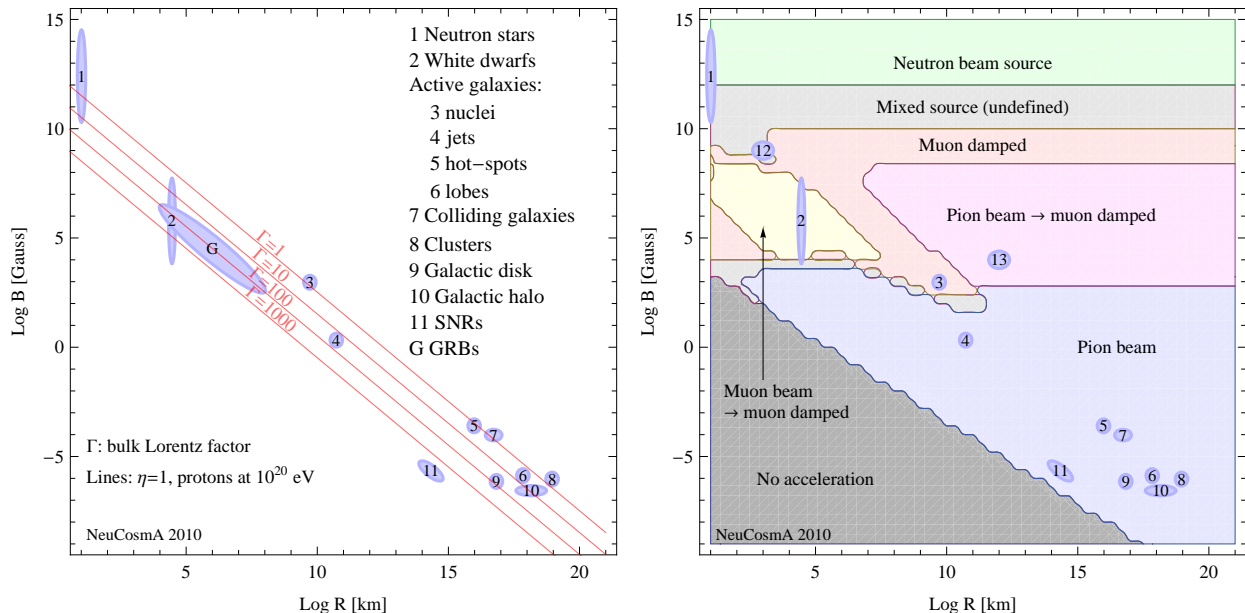


Figure 2: Left panel: Possible acceleration sites in Hillas plot as a function of R and B (version adopted from M. Boratav). Right panel: Classification of sources for injection index $\alpha = 2$ in this plot (see main text). Some points from left plot are shown for orientation, as well as two new points (12 and 13) are defined for later reference. Figure taken from Ref. [43].

boost Γ of the acceleration region into the observer’s frame must be taken into account. We stick to the interpretation of R and B in the SRF, which means that (for $\eta = 1$) the condition in Eq. (17) depends on the Lorentz boost of the source. This is illustrated by showing Eq. (17) for several selected Lorentz boosts in Fig. 2, left panel, for protons, $\eta = 1$, $E_{\text{max}} = 10^{20}$ eV. In the following, we will use $\Gamma = 1$. However, it should be noted that if the source is significantly boosted, the neutrino energies will have to be increased by Γ , and the (cascade) threshold of the neutrino telescope may be passed. We neglect redshift effects on the other hand.

In Fig. 2, right panel, the main result of Ref. [43] is shown for $\alpha = 2$: Here the sources are classified into the categories from Sec. 2 as a function of R and B . Note that a given source may fall into different categories in different energy ranges. For example, the “muon beam \rightarrow muon damped” region means that a muon beam is found for low energies, whereas a muon damped source is found for higher energies. The classical “pion beam \rightarrow muon damped” category is found for large enough magnetic fields and large enough R as well, where the transition between adiabatic and synchrotron cooling leads to an additional break in the proton spectrum.

We illustrate the classification of the sources for test point (TP) 13 from Fig. 2 (right panel), see Fig. 3, where the neutrino fluxes and flavor ratio at the source are explicitly shown for an injection index, $\alpha = 2$. One can easily see in the left panel that the different cooling and decay timescales of the secondaries lead to a hierarchy of the breaks, as described in Eq. (13), an effect which is similarly present in GRBs (see, *e.g.*, Refs. [41, 68]). The ν_e flux

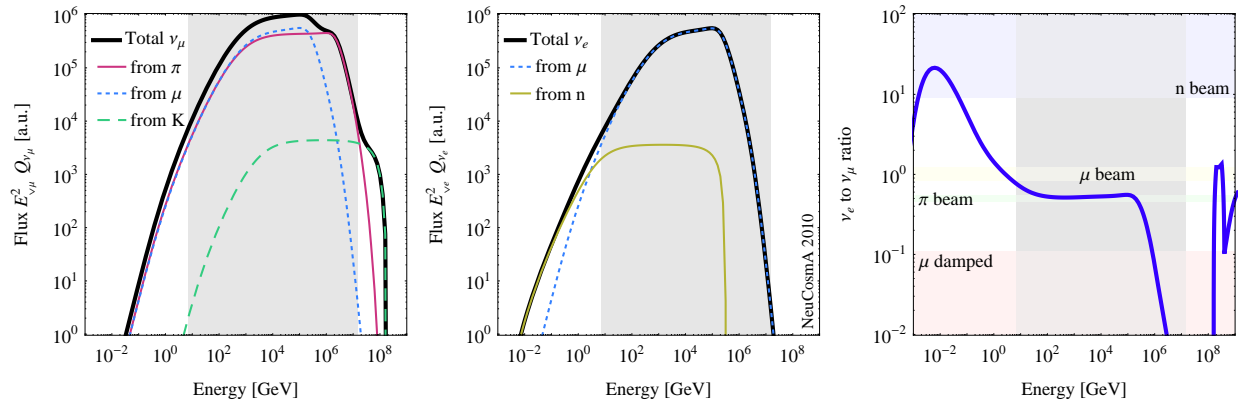


Figure 3: Muon (left panel) and electron (middle panel) neutrino fluxes at the source, and \widehat{X} (right panel) as a function of energy for test point (TP) 13 from Fig. 2, right panel. The contributions of the individual neutrino fluxes from different parents are shown as well. The gray-shaded regions mark the energy window used for the source classification (see main text). Figure adopted from Ref. [43].

mostly comes from muon decays (middle panel), which means that it will roughly follow the muon break as in the left panel, whereas ν_μ from pion and kaon decay (left panel) extend to higher energies. As a consequence, the flavor ratio \widehat{X} changes from 0.5 to 0.0 in the right panel at about 10^6 GeV. The neutrinos from neutrons, which are produced in the photohadronic interactions, lead to a ν_e flux dominating at low energies. However, in that range the total flux is already too low compared to the peak and also drowned in the atmospheric neutrino background.

Of course the above identification of different source types applies only to an energy range where the flux of at least one of the flavors is large enough, to give reasonable statistics. Since the region close to peak in $E^2\Phi_\alpha^0$ will contribute mostly to the event rates, at least in energy ranges where the neutrino effective area is proportional to E^2 , we define an energy window which captures the “upper two orders of magnitude” in the flux. That is, we compute (for each point) the maximal flux in $E^2\Phi_\alpha^0$, and derive the energy range where the flux of any flavor is at least 1% of the respective maximal flux (in $E^2\Phi_\alpha^0$). Only this energy range is considered, since otherwise the flavor ratio may be ill-defined. This energy range is marked as shaded regions in Fig. 3. In the right panel, one can also see that the flavor ratio is ill-defined above 10^8 GeV, where the fluxes are negligible. In addition, note that it is required that a specific flavor ratio category is found over at least one order of magnitude in energy within the chosen energy window.

4 Energy dependent new physics scenarios

In presence of new physics, the flavor ratio \widehat{R} not only depends on energy dependent flavor composition of the source $\widehat{X}(E)$, but also on the new physics induced energy dependent terms in the probability, see Eq. (5). We consider two specific examples of new physics here which can give rise of energy dependent effects in opposite energy regimes. Whereas neu-

trino decays are mostly present at lower energies (the lifetime is Lorentz-boosted), quantum decoherence may plausibly cause the strongest effects at higher energies. The energy dependence of source is contained in $\widehat{X}(E)$ as described in Sec. 3 while the energy dependent new physics effects lead modification of probabilities relevant for astrophysical neutrinos as described below.

4.1 Neutrino decay

Neutrino decay is usually described by an energy dependent damping of the overall oscillation probability [47] and Eq. (6) gets modified to

$$P_{\alpha\beta} = \sum_{i=1}^3 |U_{\beta i}|^2 |U_{\alpha i}|^2 D_i(E) \quad \text{with} \quad D_i(E) = \exp\left(-\hat{\alpha}_i \frac{L}{E}\right), \quad (18)$$

as the *damping coefficient*⁴. Here $\hat{\alpha}_i = m_i/\tau_i^0$ with τ_i^0 is the rest frame lifetime for mass eigenstate ν_i . Typically the neutrino lifetime is quoted as τ_i^0/m_i since m_i is unknown. From the exponential factor, the neutrinos decay if

$$\frac{\tau_i^0}{m_i} = \hat{\alpha}_i^{-1} \lesssim 10^2 \frac{L}{\text{Mpc}} \frac{\text{TeV}}{E} \text{ s eV}^{-1}. \quad (19)$$

Thus, neutrino telescopes can probe lifetimes of the order of $\sim 10^2 \text{ s eV}^{-1}$ for $L \sim 1 \text{ Mpc}$ ($\simeq 10^{14} \text{ s}$) and $E \sim 1 \text{ TeV}$. In what follows, we use the same lifetime for all mass eigenstates, $\tau_i^0/m_i \equiv \tau^0/m$ for the sake of simplicity.

In view of the rather weak direct limits on neutrino lifetime and the proposed unparticle scenarios, one can have many different mechanisms of neutrino decay. In what follows, we do not assume a particular decay scenario but consider the general case [49]. For neutrino decay, one typically distinguishes:

Visible decays One of the decay products is visible (to the neutrino detector), typically a lighter active neutrino mass eigenstate.

Invisible decays The decay products are invisible (to the neutrino detector), such as sterile neutrinos or unparticles.

In addition, we have

Incomplete decays The mass eigenstates have decayed partially, *i.e.*, $0 \leq D_i \leq 1$.

Complete decays The mass eigenstates have decayed completely, *i.e.*, $D_i \rightarrow 0$.

In our framework Eq. (18), we can describe complete or incomplete invisible decays. For a framework for visible complete decays, see Ref. [49]. For the most general framework, see Refs. [70,71]. Note that if only a single mass eigenstate is stable in complete decays, \widehat{R} does

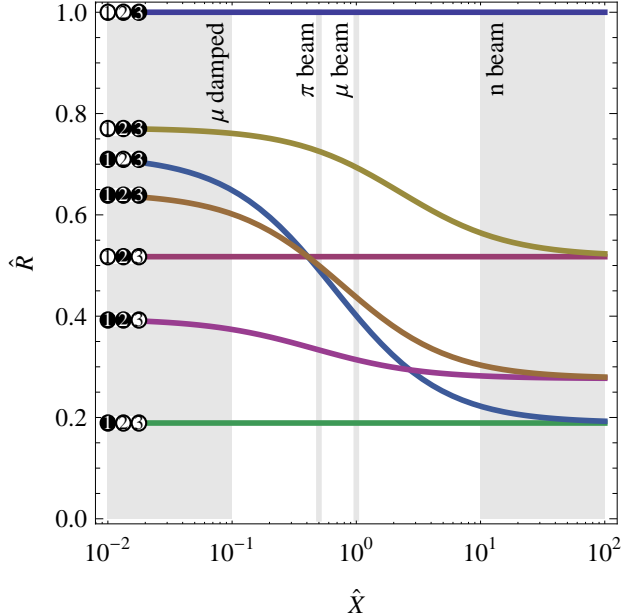


Figure 4: Flavor ratio \hat{R} as a function of \hat{X} for all complete decay scenarios. Black disks refer to stable mass eigenstates, white disks to unstable mass eigenstates. Different sources classes as a function of \hat{X} are marked.

not depend on $\hat{X}(E)$ since probabilities factorize in the source-dependent and detector-dependent parts; *cf.*, Refs. [15, 49]. In general, any decay scenario is characterized by stability properties of active states which gives in all $2^3 = 8$ scenarios for invisible decays, since each mass eigenstate can be either stable or not. We do not consider the case of only unstable states, since no signal will be observable then.

We show in Fig. 4 the flavor ratio \hat{R} as a function of \hat{X} for all complete decay scenarios. Black disks refer to stable mass eigenstates, and white disks to unstable mass eigenstates. One can read off this figure, that for the pion beam, four scenarios can be clearly separated, whereas three scenarios are almost degenerate. If, however, the information from a muon damped sources is added, such as at high energies, exactly these three scenarios, in principle, separate. The muon beam has a similar effect in the opposite direction of \hat{X} . Therefore, it is crucial to discuss sources which contain information from different parts of \hat{X} .

We show in Fig. 5 two anomalous sources described in Sec. 3: TP 3 (upper row) and TP 13 (lower row) from Fig. 2. In the left panels, the energy dependent damping coefficients D_A (for $\hat{\alpha}L = 10^6$ GeV) and D_B (for $\hat{\alpha}L = 10^8$ GeV) are shown, as well as the flavor ratio at the source $\hat{X}(E)$ ⁵. One can read off these panels, that decays become effective below

⁴In the spirit of Ref. [69], see Eqs. (2.3) and (2.4), which contain different damping effects. For astrophysical neutrinos, we can only probe $D_{ii} \equiv D_i$.

⁵Note that the chosen decay rates correspond to lifetimes of about 0.1 s eV^{-1} (D_A) and $10^{-3} \text{ s eV}^{-1}$ (D_B) for $L = 1 \text{ Mpc}$ using $\tau^0/m \sim \hat{\alpha}^{-1}$. These lifetimes are at least one order of magnitude above the current direct bounds (depending on the mass eigenstate) except from the SN 1987A bound (see, *e.g.*, Ref. [20] and references therein). It is, however, strictly speaking not trivial to assign the SN 1987A bound to ν_1 or ν_2 ,

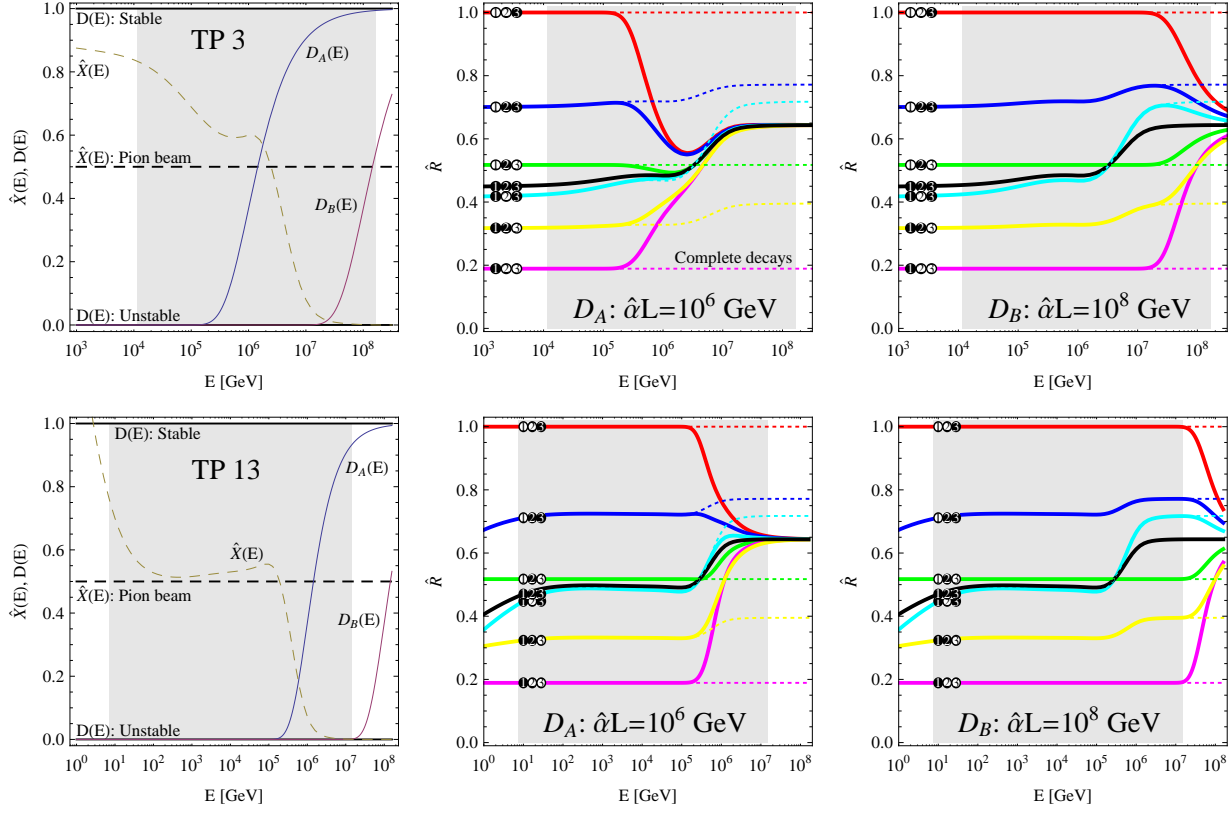


Figure 5: Left panels: Energy dependence of the damping coefficients for $\hat{\alpha}L = 10^6$ GeV (D_A) and for $\hat{\alpha}L = 10^8$ GeV (D_B), as well as for the function $\hat{X}(E)$ (dashed curves). The upper row corresponds to TP 3 from Fig. 2 (AGN nuclei), the lower row to TP 13. Middle and right panels: Energy dependence (solid curves) of the flavor ratio \hat{R} for seven different decay scenarios. Black disks refer to stable mass eigenstates, white disks to unstable mass eigenstates. The middle panels are plotted for $\hat{\alpha}L = 10^6$ GeV (D_A) and the right panels for $\hat{\alpha}L = 10^8$ GeV (D_B), where the same decay rate is chosen for all unstable mass eigenstates. The region where the flux is relatively large is shown as shaded region. The dotted curves refer to complete decays.

10^6 GeV (D_A) or 10^8 GeV (D_B) for our choice of parameters. Well above these energies, the mass eigenstates are practically stable (the lifetime increases with the Lorentz boost of the particles). The curves of $\hat{X}(E)$ clearly indicate that both the sources TP 3 and TP 13 (upper left and lower left panel) perform as muon-damped sources at high energies for which $\hat{X} \simeq 0$. At lower energies, TP 3 is undefined, whereas TP 13 performs, within reasonable uncertainty, as pion beam.

In the middle and right panels of Fig. 5, the flavor ratio \hat{R} is shown for seven different decay scenarios (solid curves). The middle panel corresponds to D_A while the right column to

given the low statistics; the problem is that a flavor eigenstate ($\bar{\nu}_e$) is measured which contains significant contributions from ν_1 and ν_2 . The only conclusion from that observation is that it is unlikely that both ν_1 and ν_2 are unstable at that energy-distance scales, which means that the upper curves in Fig. 5 (middle and right panels) are basically excluded.

D_B . As mentioned before, the same decay rate is chosen for all unstable mass eigenstates. Note that $\widehat{X}(E)$ and $\widehat{R}(E)$ have opposite behavior as a function of E . Let us first focus on plots corresponding to D_A (middle panel). From the left panel for TP 3 and TP 13, we can read off that the D_A and \widehat{X} curves intersect at about the same energy, which means that neutrino decays are only effective in the undefined (TP 3) or pion beam (TP 13) energy range below about 10^6 GeV. From Fig. 4, we know that this means that some of the decay scenarios cannot be clearly separated, which we indeed find in the lower energy range of the middle columns of Fig. 5. For $E \gg 10^6$ GeV, however, all mass eigenstates are stable, which can be seen from the deviation of the solid curves with respect to the dotted ones which refer to complete decays (independent of energy). If all mass eigenstates are stable, the same physics scenario is recovered in all cases, and no new information is added. This is different for the higher decay rate in the right column: here the muon damped nature of the source allows for a separation of the different curves in energy range $E \simeq 10^6 - 10^8$ GeV, where both the test points evolve into muon-damped source type, but the mass eigenstates are not yet stable. In this range, the degenerate curves separate out. Finally, Fig. 5 is an example for the interplay between the source characteristics $\widehat{X}(E)$ and the decay-type new physics scenario.

4.2 Quantum decoherence

The impact of quantum decoherence on the flux of high energy astrophysical neutrinos has been studied in Refs. [51,52,54,56]. We show in Appendix A how and under what conditions the oscillation probabilities presented for three neutrino flavors in this section are obtained. Under the assumption that oscillations average out over astrophysical distances, we can express the transition probability as a function of only two non-zero decoherence parameters Ψ and δ ,

$$P_{\alpha\beta} = \frac{1}{3} + \frac{1}{2}(U_{\alpha 1}^2 - U_{\alpha 2}^2)(U_{\beta 1}^2 - U_{\beta 2}^2)D_\Psi + \frac{1}{6}(U_{\alpha 1}^2 + U_{\alpha 2}^2 - 2U_{\alpha 3}^2)(U_{\beta 1}^2 + U_{\beta 2}^2 - 2U_{\beta 3}^2)D_\delta, \quad (20)$$

where D_Ψ and D_δ are the damping factors (corresponding to the eigenvalues of λ_3 and λ_8 , respectively, of the decoherence matrix described in Appendix A) given by ⁶

$$D_\kappa(E) = \exp(-2 \kappa L E^n). \quad (21)$$

Here $D_\kappa(E)$ parameterizes effects due to quantum decoherence and $U_{\alpha i}$ are the elements of the standard neutrino mixing matrix. Here n carries the energy dependent imprint of a specific model. In the literature, $n = -1, 0, 2$ have been used (see also Ref. [69]). In principle, Ψ and δ can take different values, however, in what follows we will assume the same energy dependence for the two parameters.

From Eq. (20), we note that quantum decoherence scenario *always* leads to flavor equipartition (1 : 1 : 1) as we take the asymptotic limit $L \rightarrow \infty$ if both $\Psi, \delta > 0$, whereas in the limit $\Psi, \delta \rightarrow 0$, we recover the standard oscillation result (Eq. (6)). Physically, the meaning of flavor equipartition (1 : 1 : 1) is that neutrino flavor gets completely randomized due to

⁶Note that, κ is used to denote Ψ, δ and compared to Appendix A, we incorporate the energy dependence explicitly here, *i.e.*, we replace $\Psi \rightarrow \Psi E^n, \delta \rightarrow \delta E^n$.

interaction of system with the environment and all the flavors get equally populated. This result does not depend on the particular type of source or choice of mixing parameters. However, as noted before flavor equipartition was also obtained in the standard oscillations (without decoherence) specifically for the pion beam source for the best-fit values of mixing angles. This coincidence is purely accidental and there is no physical reason for this coincidence. In order to infer effects due to quantum decoherence therefore the pion beam source is rendered useless. However, any of the anomalous sources (which do not lead to accidental flavor equipartition) are thought to be good candidates for the study of decoherence vis-a-vis standard oscillations. For instance, it is shown that detection of galactic electron anti-neutrino beams at IceCube will lead to a major improvement in sensitivity to quantum decoherence effects [52, 54, 56]. We find such a source at low energies or the extreme high- B region in Fig. 2. However, the neutrino energies are typically too low in these cases to have flavor identification in the neutrino telescopes (the extremely high magnetic field leads to proton synchrotron losses such that it is difficult to accelerate to high energies).

For a fixed value of n (which characterizes a particular model), we choose the following four cases:

1. $\delta = \Psi = 0$ (standard oscillations)
2. $\delta = \Psi > 0$
3. $\delta = 0$ and $\Psi > 0$
4. $\Psi = 0$ and $\delta > 0$

Since $n = 0$ leads to an energy-independent effect, we do not consider this case. Therefore, we study the following two cases:

- (a) $n = 2$: This corresponds to a string inspired model [60],

$$D_\kappa(E) = \exp(-2\kappa LE^2) . \quad (22)$$

Here the quantum decoherence effects are present at high energies. From the exponential factor, setting $2\kappa LE^2 \sim \mathcal{O}(1)$ we have decoherence for

$$\kappa^{-1} \lesssim 2 \times 10^{44} \frac{L}{\text{Mpc}} \left(\frac{E}{\text{TeV}} \right)^2 \text{ GeV} . \quad (23)$$

This implies that astrophysical neutrinos with $E = 1$ TeV and $L = 1$ Mpc allow us to probe $\kappa \simeq 10^{-44}$ GeV $^{-1}$ for this case.

- (b) $n = -1$: This corresponds to a Lorentz invariant model [60],

$$D_\kappa(E) = \exp\left(-2\kappa \frac{L}{E}\right) . \quad (24)$$

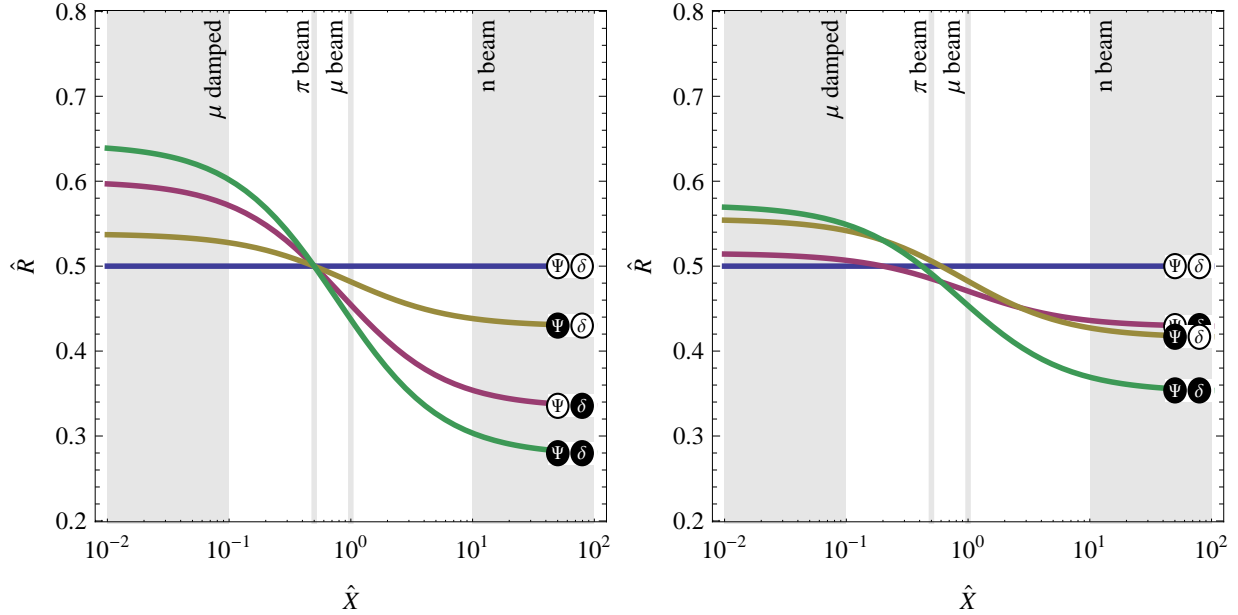


Figure 6: Flavor ratio \hat{R} as a function of \hat{X} for all complete decoherence scenarios (L large). Black disks refer to coherent parameters ($\kappa = 0$), white disks to decoherent parameters ($\kappa > 0$). Different sources classes as a function of \hat{X} are marked. Left figure is for our best-fit values of the parameters ($\sin^2 \theta_{23} = 0.5$), while the right figure is for $\sin^2 \theta_{23} = 0.4$.

Here the quantum decoherence effects are present at low energies. The spectral signature is similar to decay (Eq. (18)). From the exponential factor, setting $2\kappa L/E \sim \mathcal{O}(1)$, we have decoherence for

$$\kappa^{-1} \lesssim 2 \times 10^{35} \frac{L}{\text{Mpc}} \frac{\text{TeV}}{E} \text{ GeV}^{-2}. \quad (25)$$

This implies that astrophysical neutrinos with $E = 1$ TeV and $L = 1$ Mpc allow us to probe $\kappa \simeq 10^{-35} \text{ GeV}^2$ for this case. We note that even though decay and decoherence are two distinct physical processes, non-zero value of decoherence parameters Ψ, δ can be used to set a limit on the neutrino lifetime, from Eq. (25) we get $\hat{\alpha}^{-1} = \tau^0/m \simeq 10^2 \text{ s eV}$ for $E = 1$ TeV and $L = 1$ Mpc.

We have introduced four scenarios for decoherence, since any decoherence parameter (Ψ or δ) can be switched on or not. We show in Fig. 6 the flavor ratio \hat{R} as a function of \hat{X} for all complete decoherence scenarios, *i.e.*, the limit of large enough L . Black disks refer to coherent parameters ($\kappa = 0$), white disks to decoherent parameters ($\kappa > 0$). As for the decay, we have chosen $\delta = \Psi$ in the case where both parameters are decoherent. First of all, one can read off from this figure (left panel for maximal atmospheric mixing) that $\delta = \Psi > 0$ leads to $\hat{R} = 0.5$, irrespective of the value of \hat{X} , since universal flavor mix is a generic prediction of the decoherence scenario. This can be seen from Eq. (20). Even more surprising is the fact that all four scenarios have the same value of \hat{R} as for complete

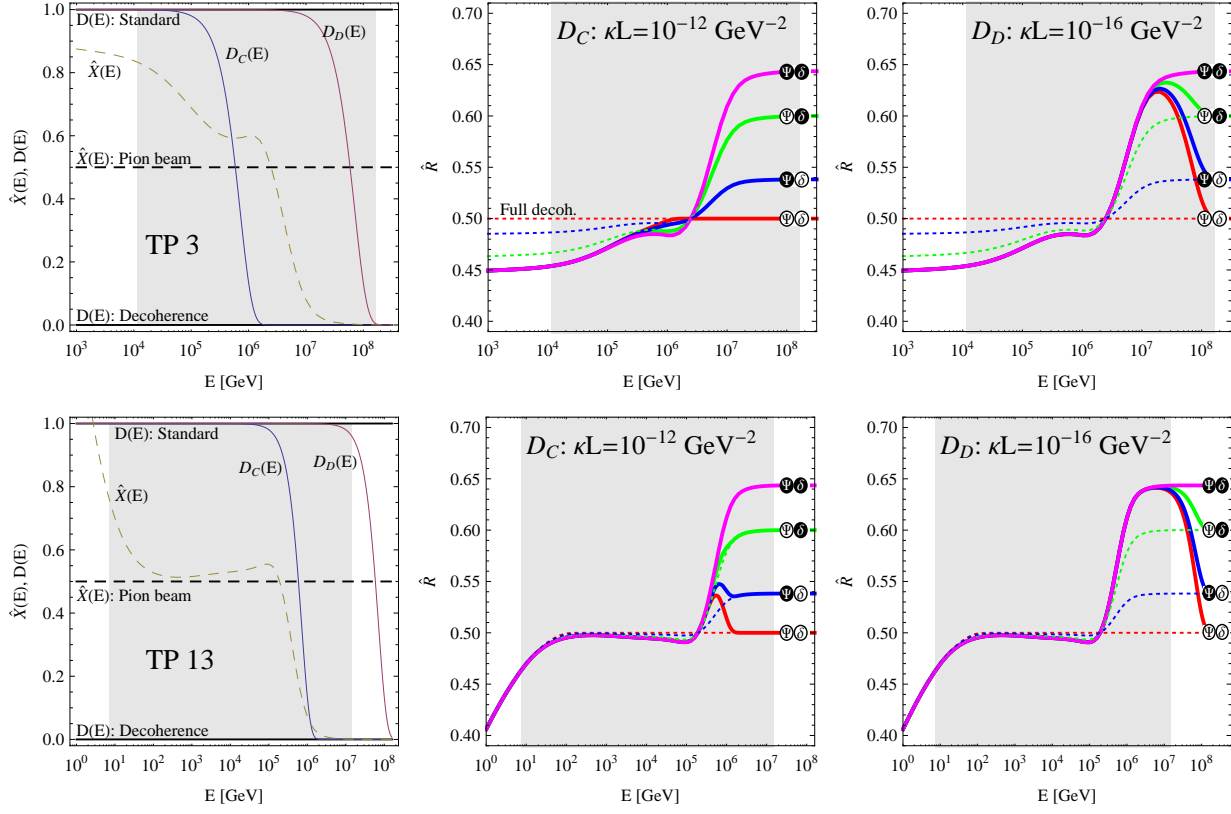


Figure 7: Left panels: Energy dependence of the decoherence coefficients for case (a) ($D_\kappa(E) = \exp(-2\kappa LE^2)$) for $\kappa L = 10^{-12} \text{ GeV}^{-2}$ (D_C) and for $\kappa L = 10^{-16} \text{ GeV}^{-2}$ (D_D), as well as for the function $\hat{X}(E)$ (dashed curves). The upper row corresponds to TP 3 from Fig. 2 (AGN nuclei), the lower row to TP 13. Middle and right panels: Energy dependence (solid curves) of the flavor ratio \hat{R} for the four different decoherence scenarios in case (a). Black disks refer to coherent parameters ($\kappa = 0$), white disks to decoherent parameters ($\kappa > 0$). The middle panels are plotted for $\kappa L = 10^{-12} \text{ GeV}^{-2}$ (D_C) and the right panels for $\kappa L = 10^{-16} \text{ GeV}^{-2}$ (D_D). The region where the flux is relatively large is shown as shaded region. The dotted curves refer to complete decoherence.

decoherence case (case 2) for the pion beam. This is actually due to the conspiracy between the use of best-fit values and the value of \hat{X} which leads to vanishing of terms dependent on the mixing matrix elements in Eq. (20) for other three cases, including that of standard oscillations (see Appendix A). If we change one of the mixing angles ($\sin^2 \theta_{23}$), the curves indeed separate out for the pion beam source (see Fig. 6, right panel). The biggest splitting is obtained for the neutron beam, whereas the scenarios can also be distinguished for the muon beam and muon damped source, in principle. In these cases, the curve $\Psi = \delta > 0$ deviates strongest from the standard case $\Psi = \delta = 0$. Note that compared to neutrino decay, all the different scenarios are relatively close to each other, which means that in practice it may be extremely difficult to disentangle them.

We show in Fig. 7, the four possible scenarios for case (a) ($n = 2$), which are qualitatively different from decay because here decoherence enters at high energies. This figure is sim-

ilar to Fig. 5, with the white (black) disks referring to decoherence (no decoherence) from the specific parameter. The middle and right panels correspond to two different values of the decoherence parameters ⁷. As expected from the energy dependence of decoherence induced damping, the main effects are present for high energies, where the scenarios differentiate thanks to the muon-damped behavior of both the test points. In these cases, they approach the “full decoherence” curves (dotted). Comparing D_C (middle panels) and D_D (right panels), D_C catches a part of the transition region between the different source types. However, since the scenarios are quite alike there, this does not help. The decoherence scenario D_D , however, leads to effects practically beyond the peak of the spectrum. Therefore, $\kappa L = 10^{-16} \text{ GeV}^{-2}$ is about the maximal sensitivity one can achieve. Comparing TP 3 (upper row) with TP 13 (lower row), one can see from the dotted curves that one could, in principle, also use the range $E \ll 10^6 \text{ GeV}$ in the upper middle panel for the case of complete decoherence. However, the decoherence effects do not show up at such low energies for the chosen parameter values.

In Fig. 8, the case (b) ($n = -1$) is shown for comparison. In this case, the energy dependence is similar to decay, and the effect of decoherence is present at lower energies. As for decay, it is very important here that the decoherence effect is large enough to catch a part of the muon-damped range. However, compared to decay, none of the scenarios are distinguishable at low energies, and one has to rely on the high energy information. In case (b) (compared to case (a)), the range for the decoherence parameters for which the scenarios (for D_E and D_F) can be distinguished, is small. For example, in the middle panels (D_E) the decoherence parameters are not large enough to produce observable effects in the muon-damped range. In the right panels (D_F), there is some energy range where the scenarios can be distinguished. At high energies, the muon-damped fixed point is then approached again by all scenarios, which is similar to decay.

5 Potential sources on Hillas plot for new physics searches

Here we discuss which source classes may be especially useful for the purpose of extraction of energy dependent new physics scenarios. We do not take into account instrumental or mixing parameter uncertainties. We also do not perform a statistical treatment, but we comment on statistics at the end of this section. We study where to look for possible new physics effects from the theoretical point of view, *i.e.*, under ideal set of assumptions.

As method, we count the number of our (seven) decay or (four) decoherence scenarios which we can uniquely determine for any energy around the spectral peak at a specific tolerance. That is, for each pair of parameters $\{R, B\}$, it is tested if the energy dependent flavor ratio can be distinguished from all other scenarios at least at some energy value (which can be

⁷For a distance of $L = 1 \text{ Mpc}$, the chosen values for case (a) ($n = 2$) correspond to $\kappa \sim 10^{-50} \text{ GeV}^{-1}$ for D_C ($\kappa L = 10^{-12} \text{ GeV}^{-2}$) and $\kappa \sim 10^{-54} \text{ GeV}^{-1}$ for D_D ($\kappa L = 10^{-16} \text{ GeV}^{-2}$) respectively. The chosen values for case (b) ($n = -1$) correspond to $\kappa \sim 10^{-32} \text{ GeV}^2$ for D_E ($\kappa L = 10^6 \text{ GeV}$) and $\kappa \sim 10^{-30} \text{ GeV}^2$ for D_F ($\kappa L = 10^8 \text{ GeV}$) respectively. Specifically, for case (a), that is about 10^{24} times more sensitive compared to terrestrial long baseline experiments, while for case (b) the sensitivity is about 10^9 times higher (see Ref. [60]). The reason for higher sensitivities is the much longer distances, and, in case (a), also the higher energies involved.

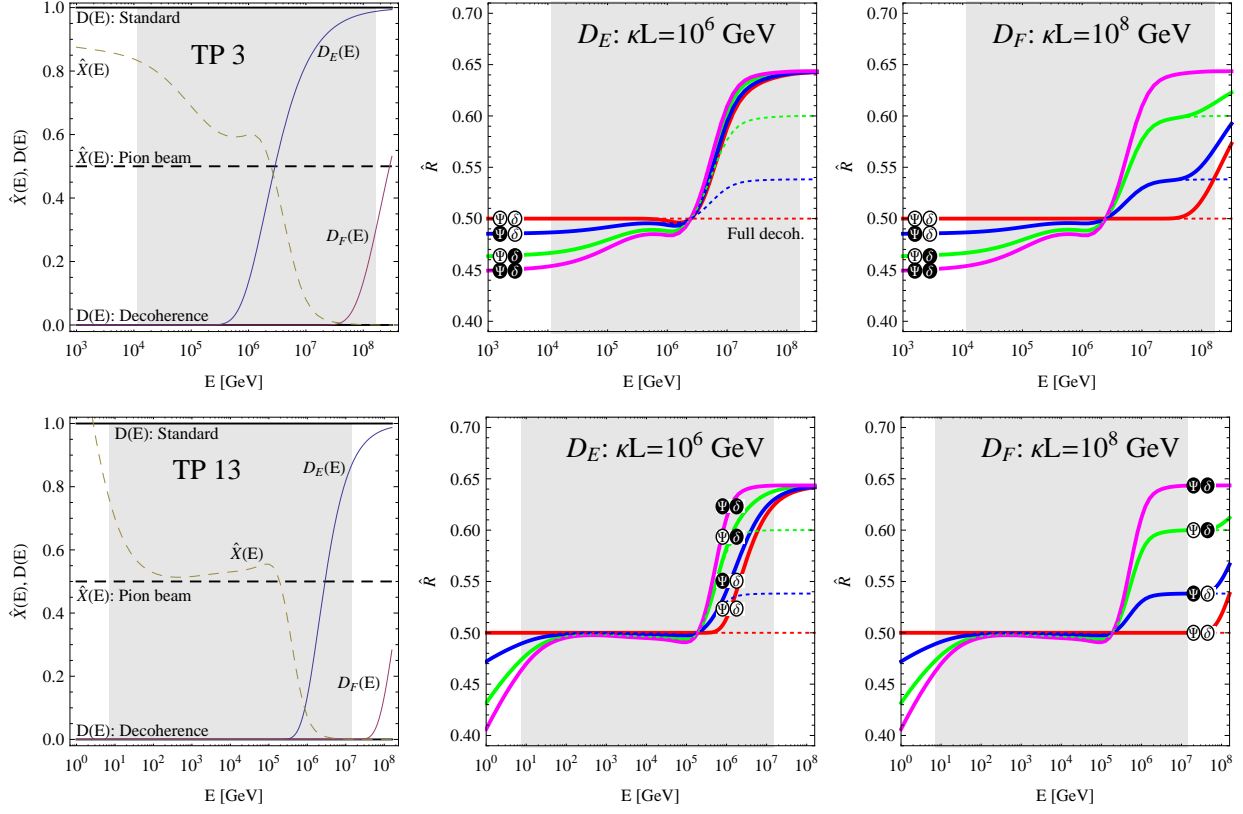


Figure 8: Left panels: Energy dependence of the decoherence coefficients for case (b) ($D_\kappa(E) = \exp(-2\kappa \frac{L}{E})$) for $\kappa L = 10^6$ GeV (D_E) and for $\kappa L = 10^8$ GeV (D_F), as well as for the function $\hat{X}(E)$ (dashed curves). The upper row corresponds to TP 3 from Fig. 2 (AGN nuclei), the lower row to TP 13. Middle and right panels: Energy dependence (solid curves) of the flavor ratio \hat{R} for the four different decoherence scenarios in case (b). Black disks refer to coherent parameters ($\kappa = 0$), white disks to decoherent parameters ($\kappa > 0$). The middle panels are plotted for $\kappa L = 10^6$ GeV (D_E) and the right panels for $\kappa L = 10^8$ GeV (D_F). The region where the flux is relatively large is shown as shaded region. The dotted curves refer to complete decoherence.

different for different scenarios). Then the number of such unique scenarios is counted. Note that compared to Fig. 2, where the source is to be found over at least one order of magnitude in energy, we also allow for smaller energy windows. In addition, note that this approach is conservative from the theoretical point of view, because even though a scenario may not be uniquely established, some other scenarios may be excluded. For the numerical analysis, we need to impose some numerical uncertainty Δ on \hat{R} (tolerance). For example, for $\Delta = 10\%$ and $\hat{R} = 0.5$ for the encountered (true) scenario, only scenarios with $\hat{R} < 0.45$ or $\hat{R} > 0.55$ can be excluded.

In Fig. 9, we show the number of decay scenarios (color coding: see legend) which can be uniquely determined as a function of R and B for $\alpha = 2$. In the left panel, the tolerance $\Delta = 10\%$, in the right panel, $\Delta = 30\%$. The lighter the color, the more scenarios can, in principle, be uniquely determined. The (light) spikes at the bottom ($R \sim 10^{15}$ km,

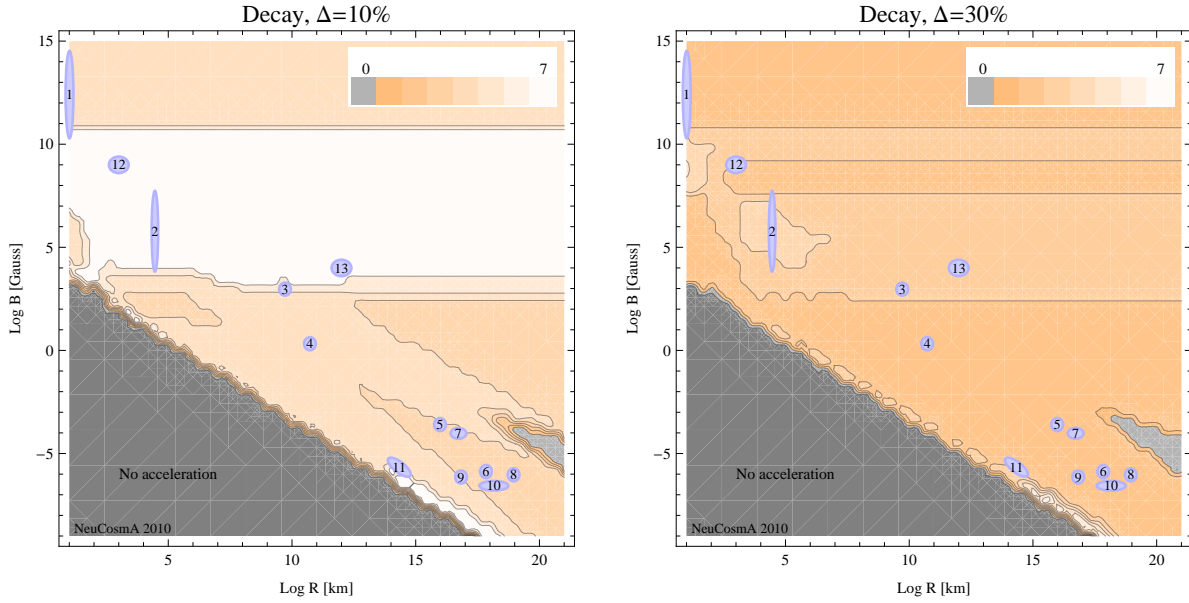


Figure 9: Number of decay scenarios (color coding: see legend) which can be uniquely determined for the model from Ref. [43] on the Hillas plot. In the left panel, the tolerance $\Delta = 10\%$, in the right panel, $\Delta = 30\%$. Here $\hat{\alpha}L = 10^8$ GeV (D_B) and $\alpha = 2$. See main text for details.

$B \sim 10^{-7}$ Gauss) come from a contribution from neutron decays. For the (dark) spike on the right sides ($R \sim 10^{21}$ km, $B \sim 10^{-5}$ Gauss), the energies around the spectral peak are already too high, *i.e.*, the neutrinos from these sources are practically stable. If the tolerance is low enough, obviously all scenarios can be identified uniquely if the magnetic field is in the range to allow for both the pion beam and the muon damped part at high energies; *cf.*, Fig. 5. If only one type of source is dominant, such as for the pion beam region in Fig. 2, not all scenarios can be disentangled. For the tolerance $\Delta = 30\%$, of course, fewer new physics scenarios can be identified. However, it is clear from Fig. 9, that the potentially interesting sources have substantial magnetic fields 10^3 Gauss $\lesssim B \lesssim 10^{11}$ Gauss, which are, however, not too high to lead to the entire domination of the neutron beam or muon damped part. For example, for our TP 3 (AGN cores), depending on the tolerance, three to six scenarios can be uniquely determined, which is already very good. Other good candidates might be white dwarfs and gamma-ray bursts (not shown here, since they are not described well within our toy model).

We show similar analysis for decoherence scenarios (a) and (b) in the left and right panels of Fig. 10, respectively. Here we have chosen a much smaller values for the tolerance ($\Delta = 5\%$), since all scenarios are very close to each other. Since the decoherence scenarios are identical for the pion beam source and split up in equally separated values of \hat{R} for the muon damped source, there is practically no qualitative effect of the number of scenarios: either all or none can be identified. For both decoherence scenarios (a) and (b), the pion beam source alone is not sufficient, as we discussed earlier, which means that substantial magnetic fields are required. As a qualitative difference between scenarios (a) and (b), (a) requires high energies for the effect due to decoherence to be present, whereas the signature

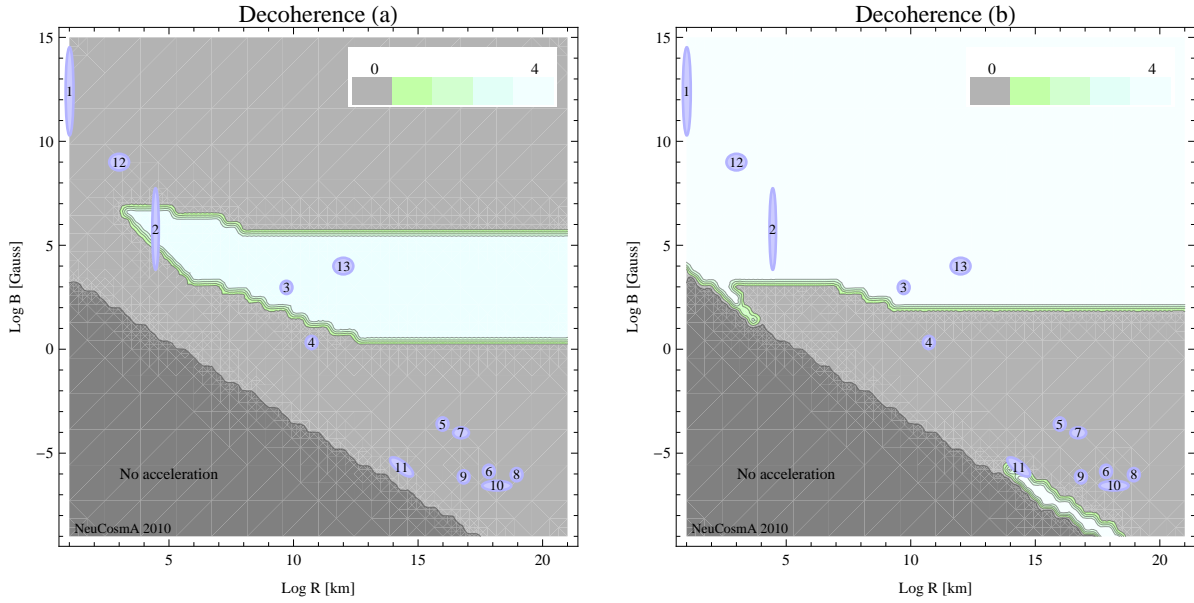


Figure 10: Number of decoherence scenarios (color coding: see legend) which can be uniquely determined for the model from Ref. [43] on the Hillas plot. In the left panel, decoherence scenario (a) is shown for $\kappa L = 10^{-12} \text{ GeV}^{-2}$ (D_C), in the right panel decoherence scenario (b) for $\kappa L = 10^8 \text{ GeV}$ (D_F). Here $\alpha = 2$ and a tolerance on the flavor ratio of 5% is assumed. See main text for details.

of (b) is strongest at low energies. Since proton synchrotron losses in the magnetic field limit the maximal energy in the considered model, the magnetic field cannot be too strong in case (a), whereas the optimal region for (b) is basically consistent with the non-pion beam region in Fig. 2. Note, however, that for too large B , the neutrino energies may not even be above the cascade threshold in an experiment such as IceCube (unless the source energies are highly Lorentz-boosted). In addition, in case (a), magnetic fields as low as 10 Gauss may be useful if $R \gtrsim 10^{12} \text{ km}$, because then high neutrino energies are obtained while magnetic field effects can be still observed. In both cases, TP 2 and TP 3 lie in the optimal region, similar to the decay example above.

In principle, one can also look into the parameter ranges in the individual scenarios which can be constrained. We find that decay and decoherence (b) prefer high magnetic fields, where the muon damped (and neutron beam) ranges are found at relatively low energies. However, again, note that in this case the event rates are surely extremely low, and that the energies may not even be above the cascade threshold in an experiment such as IceCube. On the other hand, decoherence (a) scales basically with the maximal energy allowed in the model, *i.e.*, lower B and larger R are preferred. However, as discussed, B cannot be too low (lower than about 1 Gauss), since the effect cannot be seen for the pure pion beam. Considering the optimal tradeoff between high enough neutrino energies and large enough new physics effects, probably the lightest region in Fig. 9, left, represents the parameter space of the most useful sources for new physics effects present at low energies, and the light region in Fig. 10 (left), for effects present at high energies. In the range $10^3 \text{ Gauss} \lesssim B \lesssim 10^6 \text{ Gauss}$, most distinct scenarios may be accessible.

The discussion in this section has been performed without dedicated statistical study, since it is not clear which sources will provide signals and how large these could be. The number of events N can be estimated by the convolution of the flux with the exposure (neutrino effective area times time), see, *e.g.*, Ref. [72] for the effective area of IceCube-40 for different source declinations. In the absence of backgrounds, which may be used as a first approximation for point sources using the angular resolution for background suppression, the flux limit scales inversely with N . At the 90% CL, 2.4 events are still compatible with the non-observation of a flux in about one year of IceCube-40 data. Taking into account that the effective area of IceCube-86 is about a factor of three to four higher at 100 TeV (see Ref. [73], Fig. 5) and assuming a total exposure of ten years, about 100 (muon track) events in total can still be expected in the full-scale experiment if the current bounds are saturated. The effective area for cascades, which are dominated by ν_e and ν_τ is, however, about a factor of ten lower at 100 TeV [14, 73], where it somewhat helps for statistics that we use the fluxes from both ν_e and ν_τ and do not require an unfolding of the ν_e events, as, *e.g.*, in Ref. [41]. For flavor equipartition at the detector, this means that for 100 muon tracks only 10 cascades may be expected, and that cascades may constrain the statistics. This however does not apply to all cases. For instance, if only m_1 is stable (see also Ref. [41]), $\widehat{R} \simeq 0.2$ implies that considerably more cascades than muon tracks are expected, up to 50 cascades are compatible with the current (muon track) bounds, corresponding to a statistical error of \widehat{R} of only 14%. Of course, a unique scenario identification is very difficult, but some scenarios may be excluded then (see, *e.g.*, Ref. [49] for a more detailed statistical discussion). In addition, for detectors such as the DeepCore array, more muon tracks are fully contained, which means that this discrepancy should be smaller. In Ref. [41], it was also pointed out that the detector response for muon tracks and showers depends on the spectral shape, since the energy dependence of these two event classes is different. It may be regarded as a strength of our approach that we can not only predict the flavor ratio, but also the spectral shape. Finally, mixing parameter uncertainties have not been taken into account. However, we expect that these will be reduced by future measurements on the time-scale discussed here to a level at which they are only a sub-dominant contribution to the total uncertainty, see Fig. 11 in Ref. [43].

6 Summary and discussion

We have discussed the role of flavor ratio measurements at neutrino telescopes to decipher potential new physics effects during the propagation of neutrinos. While in the literature, flavor ratios at the source are typically considered as constant numbers for particular source classes (pion beam, muon damped, muon beam, neutron beam), we have incorporated energy dependence in these flavor ratios at the source. We assume that these flavor ratios can be predicted well if the astrophysical parameters of the source are known, such as size of the acceleration region R , magnetic field B of the source, and injection index α . In many cases it is possible to estimate these parameters from the observation of the gamma-ray counterpart, such as by time variability, energy equipartition, and the spectral shape, respectively.

We have used the HMWY toy model [43] for the flux computation, which can describe relatively wide parameter regions using as few assumptions as possible. In this case, charged

mesons are produced from photohadronic interactions between protons and the synchrotron photons of co-accelerated electrons/positrons. We have emphasized that the flavor ratios for a specific energy do not depend on as many assumptions as the spectral shape. Basically, they are determined by the cooling and escape processes of the secondaries, *i.e.*, the pions, muons, kaons, and neutrons, whereas any additional cooling or escape processes of the primaries (protons, electrons, positrons) only affect the spectral shape and maximal energy. Therefore, flavor ratios may serve as the most robust prediction one may expect from an astrophysical source. However, they are much more difficult to measure: as minimal assumption, one needs to distinguish between muon tracks and cascades in a neutrino telescope. The measurement of cascades in this spirit has, for the first time, very recently been discussed in Ref. [14] for IceCube-22.

Apart from the flavor ratio at the source, new physics in the neutrino propagation may also show up as another energy dependent effect. We have used two examples for such new physics effects, (invisible) neutrino decay and quantum decoherence, to illustrate the interplay between energy dependent flavor ratios and energy dependent new physics effects. Neutrino decay characteristically shows up at low energies, where the lifetime of the particles is shortest because of the smaller Lorentz boost. Quantum decoherence, however, may plausibly be a high energy effect, at least in certain scenarios discussed in the literature. While it is useful to have different source classes as a function of energy in a neutrino source to discriminate different decay scenarios, the considered quantum decoherence prefers sources other than a pure pion beam source. The reason is that both the standard case (flavor mixing only) and the quantum decoherence (even partial decoherence) case lead to approximate flavor equilibration for the pion beam case, which means that they are indistinguishable.

As the final step, we have translated these requirements into our model parameters, where especially the magnetic field in the source plays an important role. For high magnetic fields, proton synchrotron losses limit the maximal energies, which can render high energy ($n = 2$) quantum decoherence invisible. In extreme cases, the neutrino energies may even be too low to pass the neutrino telescope threshold. For too low magnetic fields, the muon damping is not present in the flavor ratio which means that all decoherence scenarios and some decay scenarios are practically indistinguishable. Optimal magnetic fields are found to be in the range $10^3 \text{ Gauss} \lesssim B \lesssim 10^6 \text{ Gauss}$, where most effects are observable. Optimal (known) potential source classes may be AGN cores, white dwarfs, or GRBs, whereas AGN jets can only discriminate few effects as they typically perform as pion beams.

We conclude that, although tough to measure, flavor ratios are a very interesting possibility to constrain particle physics properties using astrophysical sources in parameter ranges which would be otherwise not accessible. Instead of parameterizing the flavor composition at the source by constant (energy-independent) numbers, one could take into account the energy dependence of the flavor ratio which may be indirectly obtained from the multi-messenger connection. In many new physics scenarios, it is exactly the combination of this energy dependent flavor composition and the energy dependent new physics effect which may lead to new interesting observations or constraints – even with a single source, if enough statistics can be obtained. Although a high statistics measurement may not be expected from IceCube, future neutrino telescopes may be better optimized for cascade detection.

Acknowledgments

WW acknowledges support from Deutsche Forschungsgemeinschaft, Emmy Noether grant WI 2639/2-1. PM would like to thank the Institut für Theoretische Physik und Astrophysik at Universität Würzburg for their kind hospitality during her visit in July 2010.

A Three flavor neutrino oscillation probability in presence of decoherence

Here we describe a phenomenological “bottom-up” framework to describe deviations from standard neutrino oscillation formalism in presence of decoherence irrespective of the details of the underlying theory (*e.g.*, quantum gravity). Such a quantum system is described in terms of density matrices and the Liouville equation for the neutrino flavor density matrix ρ [54–56, 74–78] (for any number of flavors) is modified to

$$\dot{\rho} = -i[H, \rho] + \mathcal{D}[\rho] \quad (26)$$

where H is the Hamiltonian and $\dot{\rho}$ implies differentiation with respect to time. The first term is responsible for unitary evolution while the term $\mathcal{D}[\rho]$ contains effects due to non-unitary evolution. A commonly used form for $\mathcal{D}[\rho]$ was given by Lindblad using quantum dynamical semi-groups [79]. For an N -level quantum system, it is possible to expand all the operators in the $SU(N)$ Hermitian basis

$$\begin{aligned} \rho &= \frac{1}{2} [p_\mu \lambda_\mu] = \frac{1}{2} [p_0 I + p_i \lambda_i] \\ H &= \frac{1}{2} [h_\mu \lambda_\mu] = \frac{1}{2} [h_0 I + h_i \lambda_i] \\ \mathcal{D}[\rho] &= \frac{1}{2} [\lambda_\mu d_{\mu\nu} \rho_\nu] \end{aligned} \quad (27)$$

which leads to the equation of motion in the component form

$$\dot{p}_\mu = (h_{\mu\nu} + d_{\mu\nu}) p_\nu \quad (28)$$

where the subscripts μ, ν depend upon the number of flavors, for three flavors, $\mu, \nu = 0, 1, \dots, 8$. The matrix elements $h_{\mu\nu}$ are usually fixed from the form of the Hamiltonian while the elements of this matrix $d_{\mu\nu}$ can be fixed by assuming that the laws of thermodynamics hold. If one imposes the requirement of the monotonic increase of von-Neumann entropy ($S = -\text{Tr}[\rho \ln \rho]$) which leads to hermiticity of operators, conservation of average value of energy, conservation of probability etc, we can further constrain the elements, $d_{\mu\nu}$. For $N = 3$ case, the basis is given by eight Gell-Mann $SU(3)$ matrices $\{\lambda_i\}$ along with the Identity I_3 matrix. We have the following matrix equation (from Eq. (28)) with eleven

decoherence parameters as in Ref. [54],

$$\frac{d}{dt} \begin{pmatrix} p_0 \\ p_1 \\ p_2 \\ p_3 \\ p_4 \\ p_5 \\ p_6 \\ p_7 \\ p_8 \end{pmatrix} = \begin{bmatrix} \begin{pmatrix} 0 & 0 & 0 & 0 & 0 & 0 & 0 & 0 & 0 \\ 0 & A & B + \omega_{21} & 0 & 0 & 0 & 0 & 0 & 0 \\ 0 & B - \omega_{21} & \Lambda & 0 & 0 & 0 & 0 & 0 & 0 \\ 0 & 0 & 0 & \Psi & 0 & 0 & 0 & 0 & 0 \\ 0 & 0 & 0 & 0 & x & y + \omega_{31} & 0 & 0 & 0 \\ 0 & 0 & 0 & 0 & y - \omega_{31} & z & 0 & 0 & 0 \\ 0 & 0 & 0 & 0 & 0 & 0 & a & b + \omega_{32} & 0 \\ 0 & 0 & 0 & 0 & 0 & 0 & b - \omega_{32} & \alpha & 0 \\ 0 & 0 & 0 & 0 & 0 & 0 & 0 & 0 & \delta \end{pmatrix} \end{bmatrix} \begin{pmatrix} p_0 \\ p_1 \\ p_2 \\ p_3 \\ p_4 \\ p_5 \\ p_6 \\ p_7 \\ p_8 \end{pmatrix}, \quad (29)$$

where $\omega_{ij} = \delta m_{ij}^2/4E$ with $\delta m_{ij}^2 = m_i^2 - m_j^2$ is the standard oscillation term. $p_0 = 2/3$ by requiring $Tr[\rho] = 1$. We impose $Tr[\rho] = 1$ and $Tr[\dot{\rho}] = 0$ which leads to conservation of probability. This leads to first row and column of the total matrix in above equation to be zero. Trace is preserved during evolution and hence p_0 remains constant. The remaining eight components of $\rho(t)$ can be obtained by solving the set of eight coupled equations subject to the initial condition

$$\rho_{\nu_\alpha}(0) = \begin{pmatrix} U_{\alpha 1}^2 & U_{\alpha 1}U_{\alpha 2} & U_{\alpha 1}U_{\alpha 3} \\ U_{\alpha 2}U_{\alpha 1} & U_{\alpha 2}^2 & U_{\alpha 2}U_{\alpha 3} \\ U_{\alpha 3}U_{\alpha 1} & U_{\alpha 3}U_{\alpha 2} & U_{\alpha 3}^2 \end{pmatrix}, \quad (30)$$

and noting that the density matrix is given by

$$\rho(t) = \frac{1}{2} \begin{pmatrix} \frac{2}{3} + p_3 + \frac{p_8}{\sqrt{3}} & p_1 - ip_2 & p_4 - ip_5 \\ p_1 + ip_2 & \frac{2}{3} - p_3 + \frac{p_8}{\sqrt{3}} & p_6 - ip_7 \\ p_4 + ip_5 & p_6 + ip_7 & \frac{2}{3} - \frac{2p_8}{\sqrt{3}} \end{pmatrix}. \quad (31)$$

The diagonal elements of $\rho(t)$ are referred to as populations while the off-diagonal elements as coherences. The phase information is contained in the coherences of the density matrix. Let us define the 8×8 block in Eq. (29) connecting the components $p_i (i \neq 0)$ by \mathcal{L}

$$\mathcal{L} = \begin{pmatrix} A & B + \omega_{21} & 0 & 0 & 0 & 0 & 0 & 0 \\ B - \omega_{21} & \Lambda & 0 & 0 & 0 & 0 & 0 & 0 \\ 0 & 0 & \Psi & 0 & 0 & 0 & 0 & 0 \\ 0 & 0 & 0 & x & y + \omega_{31} & 0 & 0 & 0 \\ 0 & 0 & 0 & y - \omega_{31} & z & 0 & 0 & 0 \\ 0 & 0 & 0 & 0 & 0 & a & b + \omega_{32} & 0 \\ 0 & 0 & 0 & 0 & 0 & b - \omega_{32} & \alpha & 0 \\ 0 & 0 & 0 & 0 & 0 & 0 & 0 & \delta \end{pmatrix} \quad (32)$$

and denote $\mathcal{M} = e^{-2\mathcal{L}t}$ and then write the solutions $p_i(t)$ in terms of the elements of exponentiated matrix \mathcal{M} ,

$$p_1(t) = p_1(0)\mathcal{M}_{11} + p_2(0)\mathcal{M}_{12} + \dots + p_8(0)\mathcal{M}_{18}$$

$$\begin{aligned}
p_2(t) &= p_1(0)\mathcal{M}_{21} + p_2(0)\mathcal{M}_{22} + \dots + p_8(0)\mathcal{M}_{28} \\
&\vdots \\
p_8(t) &= p_1(0)\mathcal{M}_{81} + p_2(0)\mathcal{M}_{82} + \dots + p_8(0)\mathcal{M}_{88} ,
\end{aligned} \tag{33}$$

where $p_i(0)$ are the components of the initial density matrix given in Eq. (30) and Eq. (31). Finally the neutrino oscillation probability $P_{\alpha\beta}$ can be computed using

$$P_{\alpha\beta}(t) = \text{Tr}[\rho_{\nu_\alpha}(t) \rho_{\nu_\beta}(0)] , \tag{34}$$

where $\rho_{\nu_\beta}(0)$ is the ‘‘pure’’ neutrino density matrix corresponding to flavor ν_β at $t = 0$ and $\rho_{\nu_\alpha}(t)$ is the density matrix at t for flavor ν_α .

For obtaining general expression of probability for astrophysical neutrinos, we need to average over sin and cos terms, which gives us

$$P_{\alpha\beta} = \frac{1}{3} + \frac{1}{2}(U_{\alpha 1}^2 - U_{\alpha 2}^2)(U_{\beta 1}^2 - U_{\beta 2}^2)D_\Psi + \frac{1}{6}(U_{\alpha 1}^2 + U_{\alpha 2}^2 - 2U_{\alpha 3}^2)(U_{\beta 1}^2 + U_{\beta 2}^2 - 2U_{\beta 3}^2)D_\delta , \tag{35}$$

where, $D_\Psi = \exp\{-2\Psi t\}$ and $D_\delta = \exp\{-2\delta t\}$ are the decoherence-induced damping factors. Thus out of the eleven decoherence parameters appearing in Eq. (29), only two (Ψ and δ) appear in the final expression which are the λ_3 and λ_8 components in the decoherence matrix. If we look at the form of $\rho(t)$, this implies that the coherences vanish for astrophysical neutrinos. This means that the rest of the physically allowed decoherence parameters are inaccessible by astrophysical neutrinos. If any of the phase information could be retained (which is what happens in atmospheric neutrino case) then the other decoherence parameters (corresponding to coherences in the $\rho(t)$) will also appear in the probability [54]. Let us now discuss the special cases in the large t limit:

- $\Psi \neq 0, \delta = 0$:

$$P_{\alpha\beta} = \frac{1}{3} + \frac{1}{6}(U_{\alpha 1}^2 + U_{\alpha 2}^2 - 2U_{\alpha 3}^2)(U_{\beta 1}^2 + U_{\beta 2}^2 - 2U_{\beta 3}^2) , \tag{36}$$

- $\Psi = 0, \delta \neq 0$:

$$P_{\alpha\beta} = \frac{1}{3} + \frac{1}{2}(U_{\alpha 1}^2 - U_{\alpha 2}^2)(U_{\beta 1}^2 - U_{\beta 2}^2) , \tag{37}$$

- $\Psi = \delta = 0$:

$$P_{\alpha\beta} = \sum_{i=1}^3 |U_{\beta i}|^2 |U_{\alpha i}|^2 . \tag{38}$$

- $\Psi = \delta \neq 0$:

$$P_{\alpha\beta} = \frac{1}{3} , \tag{39}$$

We note that only when both Ψ and δ are non-zero, one gets the equilibrium steady state value for the probability (Eq. (39)) [80]. This means that a certain combination of non-zero parameters are responsible for obtaining equilibrium steady state answer or complete irreversibility. Violation of conservation of energy in the neutrino system is necessary but not a sufficient condition to ensure this. If one of the two parameters (Ψ, δ) are zero, the probability depends upon the mixing matrix elements in general. If both the parameters (Ψ, δ) are zero, we recover standard oscillation result. We can refer to these three cases as achieving some sort of a steady state out of equilibrium.

References

- [1] J. Ahrens et al. Icecube: The next generation neutrino telescope at the south pole. *Nucl. Phys. Proc. Suppl.*, 118:388–395, 2003.
- [2] A Margiotta et al. Km3net: A cubic-kilometre scale deep sea neutrino telescope in the mediterranean sea. *Journal of Physics: Conference Series*, 203(1):012124, 2010.
- [3] F. W. Stecker, C. Done, M. H. Salamon, and P. Sommers. High-energy neutrinos from active galactic nuclei. *Phys. Rev. Lett.*, 66:2697–2700, 1991.
- [4] K. Mannheim. The proton blazar. *Astron. Astrophys.*, 269:67–76, March 1993.
- [5] A. Mücke and R. J. Protheroe. A proton synchrotron blazar model for flaring in Markarian 501. *Astropart. Phys.*, 15:121–136, 2001.
- [6] F. A. Aharonian. Proton-synchrotron radiation of large-scale jets in active galactic nuclei. *Mon. Not. R. Astron. Soc.*, 332:215–230, May 2002.
- [7] Eli Waxman and John N. Bahcall. High energy neutrinos from cosmological gamma-ray burst fireballs. *Phys. Rev. Lett.*, 78:2292–2295, 1997.
- [8] Julia K. Becker. High-energy neutrinos in the context of multimessenger physics. *Phys. Rept.*, 458:173–246, 2008.
- [9] Jorg P. Rachen and P. Meszaros. Photohadronic neutrinos from transients in astrophysical sources. *Phys. Rev.*, D58:123005, 1998.
- [10] Eli Waxman and John N. Bahcall. High energy neutrinos from astrophysical sources: An upper bound. *Phys. Rev.*, D59:023002, 1999.
- [11] Karl Mannheim, R. J. Protheroe, and Jorg P. Rachen. On the cosmic ray bound for models of extragalactic neutrino production. *Phys. Rev.*, D63:023003, 2001.
- [12] R Abbasi et al. Limits on Neutrino Emission from Gamma-Ray Bursts with the 40 String IceCube Detector. 2011.
- [13] Soebur Razzaque and A. Yu. Smirnov. Flavor conversion of cosmic neutrinos from hidden jets. *JHEP*, 03:031, 2010.

- [14] R Abbasi et al. First search for atmospheric and extraterrestrial neutrino-induced cascades with the IceCube detector. 2011.
- [15] Sandip Pakvasa. Charged lepton oscillations. *Nuovo Cim. Lett.*, 31:497, 1981.
- [16] John G. Learned and Sandip Pakvasa. Detecting tau-neutrino oscillations at PeV energies. *Astropart. Phys.*, 3:267–274, 1995.
- [17] John F. Beacom, Nicole F. Bell, Dan Hooper, Sandip Pakvasa, and Thomas J. Weiler. Measuring flavor ratios of high-energy astrophysical neutrinos. *Phys. Rev.*, D68:093005, 2003. Erratum-ibid.D72, 019901 (2005).
- [18] John F. Beacom et al. Pseudo-Dirac neutrinos, a challenge for neutrino telescopes. *Phys. Rev. Lett.*, 92:011101, 2004.
- [19] Sandip Pakvasa. Neutrino Flavor Goniometry by High Energy Astrophysical Beams. *Mod. Phys. Lett.*, A23:1313–1324, 2008.
- [20] Sandip Pakvasa. Neutrino Flavor Detection at Neutrino Telescopes and Its Uses. 2010.
- [21] Y. Farzan and A. Yu. Smirnov. Leptonic unitarity triangle and cp-violation. *Phys. Rev.*, D65:113001, 2002.
- [22] John F. Beacom, Nicole F. Bell, Dan Hooper, Sandip Pakvasa, and Thomas J. Weiler. Sensitivity to θ_{13} and δ in the decaying astrophysical neutrino scenario. *Phys. Rev.*, D69:017303, 2004.
- [23] P. D. Serpico and M. Kachelriess. Measuring the 13-mixing angle and the cp phase with neutrino telescopes. *Phys. Rev. Lett.*, 94:211102, 2005.
- [24] Pasquale D. Serpico. Probing the 2-3 leptonic mixing at high-energy neutrino telescopes. *Phys. Rev.*, D73:047301, 2006.
- [25] Pijushpani Bhattacharjee and Nayantara Gupta. Probing neutrino mixing angles with ultrahigh energy neutrino telescopes. 2005.
- [26] Walter Winter. How astrophysical neutrino sources could be used for early measurements of neutrino mass hierarchy and leptonic cp phase. *Phys. Rev.*, D74:033015, 2006.
- [27] Debasish Majumdar and Ambar Ghosal. Probing deviations from tri-bimaximal mixing through ultra high energy neutrino signals. *Phys. Rev.*, D75:113004, 2007.
- [28] Davide Meloni and Tommy Ohlsson. Neutrino flux ratios at neutrino telescopes: The role of uncertainties of neutrino mixing parameters and applications to neutrino decay. *Phys. Rev.*, D75:125017, 2007.
- [29] Werner Rodejohann. Neutrino mixing and neutrino telescopes. *JCAP*, 0701:029, 2007.
- [30] Zhi-zhong Xing. Neutrino telescopes as a probe of broken mu tau symmetry. *Phys. Rev.*, D74:013009, 2006.

- [31] Sandip Pakvasa, Werner Rodejohann, and Thomas J. Weiler. Flavor Ratios of Astrophysical Neutrinos: Implications for Precision Measurements. *JHEP*, 02:005, 2008.
- [32] Kfir Blum, Yosef Nir, and Eli Waxman. Probing cp violation in neutrino oscillations with neutrino telescopes. 2007.
- [33] Ggyoung-Riun Hwang and Kim Siyeon. Neutrino telescopes and the degeneracy problem. 2007.
- [34] Sandhya Choubey, Viviana Niro, and Werner Rodejohann. On Probing θ_{23} in Neutrino Telescopes. 2008.
- [35] Arman Esmaili and Yasaman Farzan. An Analysis of Cosmic Neutrinos: Flavor Composition at Source and Neutrino Mixing Parameters. *Nucl. Phys.*, B821:197–214, 2009.
- [36] Zhi-zhong Xing and Shun Zhou. Towards determination of the initial flavor composition of ultrahigh-energy neutrino fluxes with neutrino telescopes. *Phys. Rev.*, D74:013010, 2006.
- [37] Sandhya Choubey and Werner Rodejohann. Flavor Composition of UHE Neutrinos at Source and at Neutrino Telescopes. *Phys.Rev.*, D80:113006, 2009.
- [38] Luis A. Anchordoqui, Haim Goldberg, Francis Halzen, and Thomas J. Weiler. Neutrinos as a diagnostic of high energy astrophysical processes. *Physics Letters B*, 621(1-2):18–21, 2005.
- [39] Tamar Kashti and Eli Waxman. Flavoring astrophysical neutrinos: Flavor ratios depend on energy. *Phys. Rev. Lett.*, 95:181101, 2005.
- [40] M. Kachelriess and R. Tomas. High energy neutrino yields from astrophysical sources. I: Weakly magnetized sources. *Phys. Rev.*, D74:063009, 2006.
- [41] Paolo Lipari, Maurizio Lusignoli, and Davide Meloni. Flavor Composition and Energy Spectrum of Astrophysical Neutrinos. *Phys. Rev.*, D75:123005, 2007.
- [42] M. Kachelriess, S. Ostapchenko, and R. Tomas. High energy neutrino yields from astrophysical sources II: Magnetized sources. *Phys. Rev.*, D77:023007, 2008.
- [43] S. Hümmel, M. Maltoni, W. Winter, and C. Yaguna. Energy dependent neutrino flavor ratios from cosmic accelerators on the Hillas plot. *Astropart.Phys.*, 34:205–224, 2010.
- [44] Luis A. Anchordoqui, Haim Goldberg, Francis Halzen, and Thomas J. Weiler. Galactic point sources of TeV antineutrinos. *Phys. Lett.*, B593:42, 2004.
- [45] S. Hümmel, M. Rügner, F. Spanier, and W. Winter. Simplified models for photohadronic interactions in cosmic accelerators. *Astrophys.J.*, 721:630–652, 2010.
- [46] A. Mücke, Ralph Engel, J.P. Rachen, R.J. Protheroe, and Todor Stanev. SOPHIA: Monte Carlo simulations of photohadronic processes in astrophysics. *Comput.Phys.Commun.*, 124:290–314, 2000.

- [47] John F. Beacom, Nicole F. Bell, Dan Hooper, Sandip Pakvasa, and Thomas J. Weiler. Decay of high-energy astrophysical neutrinos. *Phys. Rev. Lett.*, 90:181301, 2003.
- [48] Debasish Majumdar. Unparticle decay of neutrinos and its effect on ultra high energy neutrinos. 2007.
- [49] Michele Maltoni and Walter Winter. Testing neutrino oscillations plus decay with neutrino telescopes. *JHEP*, 07:064, 2008.
- [50] Atri Bhattacharya, Sandhya Choubey, Raj Gandhi, and Atsushi Watanabe. Diffuse Ultra-High Energy Neutrino Fluxes and Physics Beyond the Standard Model. *Phys. Lett.*, B690:42–47, 2010.
- [51] Atri Bhattacharya, Sandhya Choubey, Raj Gandhi, and Atsushi Watanabe. Ultra-high neutrino fluxes as a probe for non-standard physics. *JCAP*, 1009:009, 2010.
- [52] Dan Hooper, Dean Morgan, and Elizabeth Winstanley. Probing quantum decoherence with high-energy neutrinos. *Phys. Lett.*, B609:206–211, 2005.
- [53] M. Bustamante, A.M. Gago, and C. Pena-Garay. Energy-independent new physics in the flavour ratios of high-energy astrophysical neutrinos. *JHEP*, 1004:066, 2010.
- [54] Dan Hooper, Dean Morgan, and Elizabeth Winstanley. Lorentz and CPT invariance violation in high-energy neutrinos. *Phys. Rev.*, D72:065009, 2005.
- [55] Dean Morgan, Elizabeth Winstanley, Jurgen Brunner, and Lee F. Thompson. Probing quantum decoherence in atmospheric neutrino oscillations with a neutrino telescope. *Astropart. Phys.*, 25:311–327, 2006.
- [56] Luis A. Anchordoqui, Haim Goldberg, M. C. Gonzalez-Garcia, Francis Halzen, Dan Hooper, Subir Sarkar, and Thomas J. Weiler. Probing planck scale physics with icecube. *Phys. Rev. D*, 72(6):065019, Sep 2005.
- [57] Zhi zhong Xing and Shun Zhou. Implications of leptonic unitarity violation at neutrino telescopes. *Physics Letters B*, 666(2):166 – 172, 2008.
- [58] Shin’ichiro Ando, Marc Kamionkowski, and Irina Mocioiu. Neutrino Oscillations, Lorentz/CPT Violation, and Dark Energy. *Phys. Rev.*, D80:123522, 2009.
- [59] Mattias Blennow and Davide Meloni. Non-standard interaction effects on astrophysical neutrino fluxes. *Phys. Rev.*, D80:065009, 2009.
- [60] Nick E. Mavromatos, Anselmo Meregaglia, Andre Rubbia, Alexander Sakharov, and Sarben Sarkar. Quantum-Gravity Decoherence Effects in Neutrino Oscillations: Expected Constraints From CNGS and J-PARC. *Phys. Rev.*, D77:053014, 2008.
- [61] R. Abbasi, Y. Abdou, M. Ackermann, J. Adams, M. Ahlers, K. Andeen, J. Auffenberg, X. Bai, M. Baker, S. W. Barwick, R. Bay, J. L. Bazo Alba, K. Beattie, S. Bechet, J. K. Becker, K.-H. Becker, M. L. Benabderrahmane, J. Berdermann, P. Berghaus, D. Berley, E. Bernardini, D. Bertrand, D. Z. Besson, M. Bissok, E. Blaufuss, D. J.

Boersma, C. Bohm, J. Bolmont, S. Böser, O. Botner, L. Bradley, J. Braun, D. Breder, T. Burgess, T. Castermans, D. Chirkin, B. Christy, J. Clem, S. Cohen, D. F. Cowen, M. V. D’Agostino, M. Danninger, C. T. Day, C. De Clercq, L. Demirörs, O. Depaepe, F. Descamps, P. Desiati, G. de Vries-Uiterweerd, T. DeYoung, J. C. Diaz-Velez, J. Dreyer, J. P. Dumm, M. R. Duvoort, W. R. Edwards, R. Ehrlich, J. Eisch, R. W. Ellsworth, O. Engdegård, S. Euler, P. A. Evenson, O. Fadiran, A. R. Fazely, T. Feusels, K. Filimonov, C. Finley, M. M. Foerster, B. D. Fox, A. Franckowiak, R. Franke, T. K. Gaisser, J. Gallagher, R. Ganugapati, L. Gerhardt, L. Gladstone, A. Goldschmidt, J. A. Goodman, R. Gozzini, D. Grant, T. Griesel, A. Groß, S. Grullon, R. M. Gunasingha, M. Gurtner, C. Ha, A. Hallgren, F. Halzen, K. Han, K. Hanson, Y. Hasegawa, J. Heise, K. Helbing, P. Herquet, S. Hickford, G. C. Hill, K. D. Hoffman, K. Hoshina, D. Hubert, W. Huelsnitz, J.-P. Hülß, P. O. Hulth, K. Hultqvist, S. Hussain, R. L. Imlay, M. Inaba, A. Ishihara, J. Jacobsen, G. S. Japaridze, H. Johansson, J. M. Joseph, K.-H. Kampert, A. Kappes, T. Karg, A. Karle, J. L. Kelley, P. Kenny, J. Kiryluk, F. Kislak, S. R. Klein, S. Klepser, S. Knops, G. Kohnen, H. Kolanoski, L. Köpke, M. Kowalski, T. Kowarik, M. Krasberg, K. Kuehn, T. Kuwabara, M. Labare, K. Laihem, H. Landsman, R. Lauer, H. Leich, D. Lennarz, A. Lucke, J. Lundberg, J. Lünemann, J. Madsen, P. Majumdar, R. Maruyama, K. Mase, H. S. Matis, C. P. McParland, K. Meagher, M. Merck, P. Mészáros, E. Middell, N. Milke, H. Miyamoto, A. Mohr, T. Montaruli, R. Morse, S. M. Movit, K. München, R. Nahnauer, J. W. Nam, P. Nießen, D. R. Nygren, S. Odrowski, A. Olivas, M. Olivo, M. Ono, S. Panknin, S. Patton, C. Pérez de los Heros, J. Petrovic, A. Piegsa, D. Pieloth, A. C. Pohl, R. Porrata, N. Potthoff, P. B. Price, M. Prikockis, G. T. Przybylski, K. Rawlins, P. Redl, E. Resconi, W. Rhode, M. Ribordy, A. Rizzo, J. P. Rodrigues, P. Roth, F. Rothmaier, C. Rott, C. Roucelle, D. Rutledge, D. Ryckbosch, H.-G. Sander, S. Sarkar, K. Satalecka, S. Schlenstedt, T. Schmidt, D. Schneider, A. Schukraft, O. Schulz, M. Schunck, D. Seckel, B. Semburg, S. H. Seo, Y. Sestayo, S. Seunarine, A. Silvestri, A. Slipak, G. M. Spiczak, C. Spiering, T. Stanev, G. Stephens, T. Stezelberger, R. G. Stokstad, M. C. Stoufer, S. Stoyanov, E. A. Strahler, T. Straszheim, K.-H. Sulanke, G. W. Sullivan, Q. Swillens, I. Taboada, O. Tarasova, A. Tepe, S. Ter-Antonyan, C. Terranova, S. Tilav, M. Tluczykont, P. A. Toale, D. Tosi, D. Turčan, N. van Eijndhoven, J. Vandenbroucke, A. Van Overloop, B. Voigt, C. Walck, T. Waldenmaier, M. Walter, C. Wendt, S. Westerhoff, N. Whitehorn, C. H. Wiebusch, A. Wiedemann, G. Wikström, D. R. Williams, R. Wischnewski, H. Wissing, K. Woschnagg, X. W. Xu, G. Yodh, and S. Yoshida. Determination of the atmospheric neutrino flux and searches for new physics with amanda-ii. *Phys. Rev. D*, 79(10):102005, May 2009.

- [62] A. M. Hillas. The Origin of Ultrahigh-Energy Cosmic Rays. *Ann. Rev. Astron. Astrophys.*, 22:425–444, 1984.
- [63] Soebur Razzaque, Peter Meszaros, and Eli Waxman. TeV neutrinos from core collapse supernovae and hypernovae. *Phys. Rev. Lett.*, 93:181101, 2004.
- [64] Rikard Enberg, Mary Hall Reno, and Ina Sarcevic. High energy neutrinos from charm in astrophysical sources. *Phys. Rev. D*, 79(5):053006, Mar 2009.

- [65] Dan Hooper, Andrew Taylor, and Subir Sarkar. The impact of heavy nuclei on the cosmogenic neutrino flux. *Astropart. Phys.*, 23:11–17, 2005.
- [66] Maximo Ave, N. Busca, Angela V. Olinto, Alan A. Watson, and T. Yamamoto. Cosmogenic neutrinos from ultra-high energy nuclei. *Astropart. Phys.*, 23:19–29, 2005.
- [67] Thomas Schwetz, M. A. Tortola, and Jose W. F. Valle. Three-flavour neutrino oscillation update. *New J. Phys.*, 10:113011, 2008.
- [68] Philipp Baerwald, Svenja Hümmer, and Walter Winter. Magnetic Field and Flavor Effects on the Gamma-Ray Burst Neutrino Flux. 2010.
- [69] Mattias Blennow, Tommy Ohlsson, and Walter Winter. Damping signatures in future neutrino oscillation experiments. *JHEP*, 06:049, 2005.
- [70] Manfred Lindner, Tommy Ohlsson, and Walter Winter. A combined treatment of neutrino decay and neutrino oscillations. *Nucl. Phys.*, B607:326–354, 2001.
- [71] Manfred Lindner, Tommy Ohlsson, and Walter Winter. Decays of supernova neutrinos. *Nucl. Phys.*, B622:429–456, 2002.
- [72] R. Abbasi et al. Time-Integrated Searches for Point-like Sources of Neutrinos with the 40-String IceCube Detector. 2010.
- [73] A. Karle and for the IceCube Collaboration. IceCube. 2010.
- [74] John Ellis, John S. Hagelin, D. V. Nanopoulos, and M. Srednicki. Search for violations of quantum mechanics. *Nuclear Physics B*, 241(2):381 – 405, 1984.
- [75] Thomas Banks, Leonard Susskind, and Michael E. Peskin. Difficulties for the evolution of pure states into mixed states. *Nuclear Physics B*, 244(1):125 – 134, 1984.
- [76] Jun Liu. Evolution of pure states into mixed states. 1993.
- [77] F. Benatti and R. Floreanini. Open system approach to neutrino oscillations. *JHEP*, 02:032, 2000.
- [78] Tommy Ohlsson. Equivalence between neutrino oscillations and neutrino decoherence. *Phys. Lett.*, B502:159–166, 2001.
- [79] G. Lindblad. On the generators of quantum dynamical semigroups. *Comm. Math. Phys.*, 48:119, 1976.
- [80] A. K. Rajagopal. The principle of detailed balance and the lindblad dissipative quantum dynamics. *Physics Letters A*, 246(3-4):237 – 241, 1998.